

Impact of Tibetan Plateau Surface Heating on Persistent Extreme Precipitation Events in Southeastern China

BINGCHENG WAN

State Key Laboratory of Atmospheric Boundary Layer Physics and Atmospheric Chemistry, Institute of Atmospheric Physics, Chinese Academy of Sciences, and University of Chinese Academy of Sciences, Beijing, China

ZHIQIU GAO

State Key Laboratory of Atmospheric Boundary Layer Physics and Atmospheric Chemistry, Institute of Atmospheric Physics, Chinese Academy of Sciences, Beijing, and Nanjing University of Information Science and Technology, Nanjing, China

FEI CHEN

National Center for Atmospheric Research, Boulder, Colorado, and State Key Laboratory of Severe Weather, Chinese Academy of Meteorological Sciences, Beijing, China

CHUNGU LU

National Science Foundation, Directorate for Geosciences, Division of Atmospheric and Geospace Science, Arlington, Virginia

(Manuscript received 9 March 2017, in final form 15 May 2017)

ABSTRACT

This paper combines observations, climatic analysis, and numerical modeling to investigate the Tibetan Plateau's (TP) surface heating conditions' influence on extreme persistent precipitation events (PEPEs) in southeastern China. Observations indicated an increase of TP surface air temperature 3–4 days prior to extreme persistent precipitation events in southeastern China. NCEP reanalysis data revealed a significant low pressure anomaly in southern China and a high pressure anomaly in northern China during extreme persistent precipitation event periods. Using correlation analysis and random resampling nonparametric statistics, a typical PEPE event from 17 to 25 June 2010 was selected for numerical simulation. The Weather Research and Forecasting (WRF) Model was used to investigate the impact of the TP's surface heating on the evolution of this event. Three contrasting WRF experiments were conducted with different surface heating strengths by changing initial soil moisture over the TP. Different soil conditions generate different intensities of surface sensible heat fluxes and boundary layer structures over the TP resulting in two main effects on downstream convective rainfall: modulating large-scale atmospheric circulations and modifying the water vapor transport at southern China. Increased surface heating in the TP strengthens a high pressure system over the Yangtze Plain, thereby blocking the northward movement of precipitation. It also enhances the water vapor transport from the South China Sea to southern China. The combined effects substantially increase precipitation over most of the southeastern China region.

1. Introduction

The Tibetan Plateau (TP), the highest plateau on Earth, plays an important role in global and regional climate, especially enhancing the East Asian summer monsoon that brought abundant precipitation to China, Korea, and Japan (Zhisheng et al. 2001; Liu and Yin 2002; Jiang et al. 2008). The TP acts as the primary

heating source before the rainy season (Yanai et al. 1992; Ye and Wu 1998) and greatly influences the onset of East Asian summer monsoon and the precipitation intensity over China (Wu and Zhang 1998). Without the TP, the monsoon would be much weaker and the precipitation over East Asia would be decreased (Jiang et al. 2008). The TP causes two main influences. One is the topographic effect, whereby the TP acts as a huge obstacle that hinders the wind flow. The second is its thermal effect, whereby the TP acts as a huge heat

Corresponding author: Dr. Zhiqiu Gao, zgao@mail.iap.ac.cn

source (Duan and Wu 2005). While the topographic effect is claimed to be the major mechanism (Boos and Kuang 2010), its thermal mechanism is also believed to play an important role (Duan and Wu 2005; Wu et al. 2012b). A decrease of TP surface wind speed has been observed since 1970 and likely contributes to the reduction in surface sensible heat flux (Duan and Wu 2008, 2009; Liu et al. 2012), which is correlated with the weakening of Asian summer monsoon and the decrease in summer precipitation over northern South Asia and northern China but an increase in precipitation over northwestern China, southern China, and Korea (Liu et al. 2012; Duan et al. 2013). In addition, TP surface wind speed reduction is linked to the increasing frequency of droughts in northern China along with the increased flooding of the Yangtze Plain (Yu et al. 2004).

Many factors may have contributed to the weakening of the Asian summer monsoon such as changes in sea surface temperature, global warming, increased pollution, and the thermal contrast of land-sea temperature (Li et al. 2010; Duan et al. 2011; Wu et al. 1997, 2012a; Zuo et al. 2013; Xu et al. 2015). Nevertheless, modeling results showed that TP's surface heating did impact the Asian summer monsoon circulations and the location of the rain belt over China (Wang et al. 2008; Liu et al. 2012; Wang et al. 2014). Weaker surface heating resulted in a weaker near-surface cyclonic circulation surrounding the plateau. The convergence of water vapor transport is confined in southern China forming a unique anomaly pattern in summer monsoon precipitation, the so-called south wet and north dry (Liu et al. 2012).

Persistent extreme precipitation events (PEPEs), like other extreme weather events, have been occurring with increasing frequency over the past several decades (Easterling et al. 2000; Kunkel et al. 2003, 2012), and southern China is no exception (Kunkel et al. 2003, 2012; Wang and Zhou 2005; Chen and Zhai 2013). Adequate safety measures can be taken if such events could be predicted. Most PEPEs in China occur during the summer. The East Asian summer monsoon and hurricane season can contribute to high rainfall in China. The TP's impact on those short-term PEPEs is unknown and may differ from the role it plays seasonally.

Development of persistent precipitation often needs persistent synoptic systems, such as stationary fronts, to build. Many studies focused on the role of sea surface temperature and intraseasonal oscillation in persistent precipitation in China (Jones 2000; Liu et al. 2008; Mao et al. 2010; Lee et al. 2013; Pan et al. 2013; Ren et al. 2013). The sea surface temperature pattern over the western Pacific Ocean is highly influenced by the location of subtropical high pressure systems, which significantly impact the abundance and location of precipitation in

China (Ding and Chan 2005; Li et al. 2001). Another important factor is the role of land surface processes, which provides surface heat fluxes to drive the evolution of the planetary boundary layer (PBL) and summer convective precipitation (Mintz 1982; Pan et al. 1996; Chen and Dudhia 2001; Stéfanon et al. 2014). Land surface heat fluxes can affect the trigger mechanism of summer rainfall and distribution of water vapor, and different initial soil conditions could lead to different weather conditions (Fennessy and Shukla 1999; Trier et al. 2004, 2011; Lawrence and Slingo 2005). This paper focuses on the TP's land surface process and investigates its relationship to PEPEs in southeastern China. Historical observation data are used to explore whether the TP surface possesses any anomaly signals during the PEPE period. Then, a case study is conducted with WRF to assess physical mechanism behind the relationship, if any. Section 2 introduces the datasets and the identification of PEPE. Section 3 gives some historical analysis for the PEPEs we chose and the process of choosing a specific case. Section 4 describes the numerical models and model experiments used in this paper. Section 5 discusses modeling results and section 6 provides a summary and discussion.

2. Datasets and identification of PEPE

The data used for this study include historical observations of daily 2-m air temperature and daily precipitation from 756 stations throughout China. A total of 113 of these stations are over the TP (Fig. 1). The data were obtained from the China Meteorological Data Service Center (2008). Long-term daily and monthly mean of the 2.5° National Centers for Environmental Prediction–National Center of Atmospheric Research (NCEP–NCAR) reanalysis data (Kalnay et al. 1996) were used for historical analyses to reveal general features of the PEPEs in southeastern China. The 3-hourly 0.25° real-time Tropical Rainfall Measuring Mission Multisatellite (TRMM 3B42 RT) Precipitation Analysis data (Huffman and Bolvin 2017) were also used. Initial and lateral boundary conditions for WRF were taken from the 6-hourly 1° NCEP Final Operational Global Analysis (FNL) data (NOAA/NWS/NCEP 2000). The 3-hourly 0.25° global land data assimilation system data products (Rodell et al. 2004) were used as land surface forcing data to drive the High-Resolution Land Data Assimilation System (HRLDAS; Chen et al. 2007).

While there are many definitions of PEPEs, here we used the definitions and results given by Chen and Zhai (2013). First, they defined a “station PEPE” as an observation station that experiences a precipitation event of amounts exceeding 50 mm for at least three

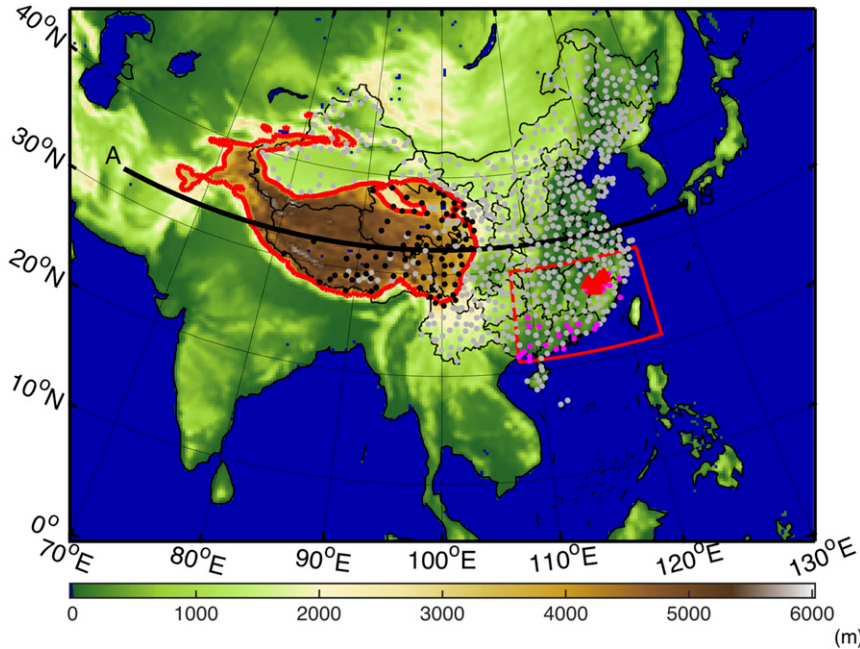


FIG. 1. The shaded color is the altitude of the simulation area. The curved red area is the contour of 3000-m altitude. The red rectangle is the focused rain area in southern China (21° – 30° N, 108° – 123° E). The transect AB (black line) is the cross-sectional line for model analysis in Fig. 11. Dots are the 756 stations spread around China: Black dots are the 87 stations with data integrity greater than 90% over the Tibetan Plateau, magenta dots are stations that experienced at least one PEPE after 1990, and gray dots are all the other stations. Red triangles are the stations that experienced the PEPE in the study period (17–25 Jun 2010).

consecutive days and ends when daily precipitation amounts to less than 50 mm for the following two consecutive days. This rule will allow the precipitation event to cease for, at most, one day before continuing. A “regional PEPE” is identified as a region containing at least three rain gauge stations that experienced station PEPE, and those precipitation events must have at least one day of temporal overlap. The neighboring stations experiencing station PEPE in the region must be less than 200 km from each other. Using these rules, Chen and Zhai (2013) identified 74 regional PEPEs from 1954 to 2010 using the same station observation data as the dataset used for this paper.

In this study, we focused on PEPEs that happened south of 30° N and east of 108° E, which is mainly the southeastern portion of China. The approximate latitude of the Yangtze River is 30° N and the approximate longitude of the boundary point between China and the Indo-China Peninsula on the coast is 108° E. Cases that occurred west of 108° E were inland; the synoptic system and water vapor supply may differ from other cases occurring alongside the coast. For all the summer PEPEs we only focused on cases occurring near the coast, but many cases were associated with tropical cyclones. For this study, all cases that happened during a

typhoon period in the South China Sea or in the East China Sea were removed. After removing those PEPEs influenced by tropical cyclones, there were 10 PEPEs between June and August from 1990 to 2010. Details for those 10 PEPEs, such as starting date and impacted area, are listed in Table 1. Stations in southern China that experienced PEPEs are shown as magenta points in Fig. 1. All these cases occurred from mid-June to early July when the Yangtze Plain is influenced by the mei-yu (Ding 1992).

3. Historical analyses and cases chosen

Even though there are 113 surface observation stations over TP, the quality of data differs greatly among stations, and many stations have missing data. We chose 87 stations (black dots in Fig. 1) having greater than 90% temporal coverage integrity during 1981–2010, and calculated the long-term daily mean 2-m air temperature. The reason for choosing 1981–2010 is to maintain temporal consistency with the reanalysis data because NCEP–NCAR (NCEP Climate Prediction Center and UCAR Joint Office for Science Support 2000) reanalysis data derived its long-term daily mean and monthly mean during 1981–2010.

TABLE 1. Precipitation cases used in this paper. Boldface font at bottom indicates the selected case.

Year	Start date	End date	No. of days	No. of stations	North ($^{\circ}$ N)	South ($^{\circ}$ N)	West ($^{\circ}$ E)	East ($^{\circ}$ E)	Max precipitation (mm)	Min precipitation (mm)
1992	4 Jul	8 Jul	5	4	28.04	25.31	117.28	119.47	447.90	215.30
1994	13 Jun	17 Jun	5	3	25.13	22.21	109.24	110.56	583.90	306.00
1997	2 Jul	9 Jul	8	3	24.12	22.32	110.31	114.00	434.70	288.60
2000	9 Jun	12 Jun	4	6	28.04	25.31	118.02	120.12	376.50	204.20
2000	17 Jul	22 Jul	6	6	23.20	21.44	108.21	113.50	435.00	230.80
2002	14 Jun	17 Jun	4	3	26.54	26.39	116.20	118.10	551.30	378.80
2005	18 Jun	24 Jun	7	9	27.55	23.48	114.44	120.12	706.80	295.10
2006	4 Jun	7 Jun	4	5	28.04	26.55	116.39	119.08	421.10	219.00
2008	7 Jul	12 Jul	6	3	23.24	21.44	112.46	116.41	323.90	288.80
2010	17 Jun	25 Jun	9	5	27.55	26.54	116.39	118.32	754.40	441.10

To analyze the TP surface air temperature features and associated anomalies during the PEPEs period, we synchronized the 10 cases by setting their starting times as the onset time. For each case, we calculated the 87 stations' average 2-m air temperatures over TP and their long-term daily mean temperatures during the same period of the year. The same method was applied to the 126 stations in southeastern China inside the red rectangle in Fig. 1 to derive the area-averaged precipitation. Results are shown in Fig. 2. The second maximum and minimum temperature and precipitation of the 10 cases were also plotted to show the spread of the 10 cases. The

2-m air temperature over the TP shows a clear warm anomaly prior to the PEPE's onset and throughout the duration of the PEPEs. According to the observation dataset from the China Meteorological Data Service Center, the daily precipitation was measured from 2000 LST the day before to 2000 LST of the measured day. The daily 2-m air temperature is obtained by averaging observations from four time periods (0200, 0800, 1400, and 2000 LST), so the precipitation data are 4 h ahead of the 2-m air temperature. Figure 2 shows that the PEPE started about 3–4 days after the TP surface temperature warm anomaly reached $1^{\circ}\text{--}2^{\circ}\text{C}$, and peaked on

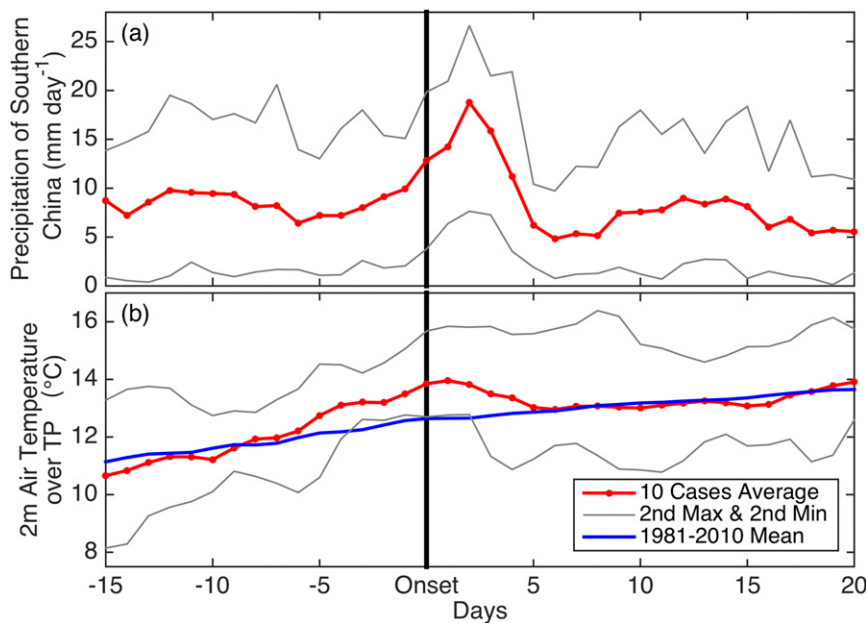


FIG. 2. Time series of mean precipitation and 2-m air temperature for the 10 PEPEs selected in this study. (a) Temporal and spatial average precipitation over the 126 southern China stations in the red rectangle in Fig. 1. The x axis represents days from onset. Onset is the starting day of PEPE. (b) Temporal and spatial average of 2-m air temperature of the 87 stations over TP. Gray lines represent the second maximum and second minimum of the 10 chosen cases. The second maximum and second minimum represent the 10th and 90th percentile cases, respectively. Red lines represent the 10 chosen cases and blue lines indicate the 1981–2010 daily long-term means.

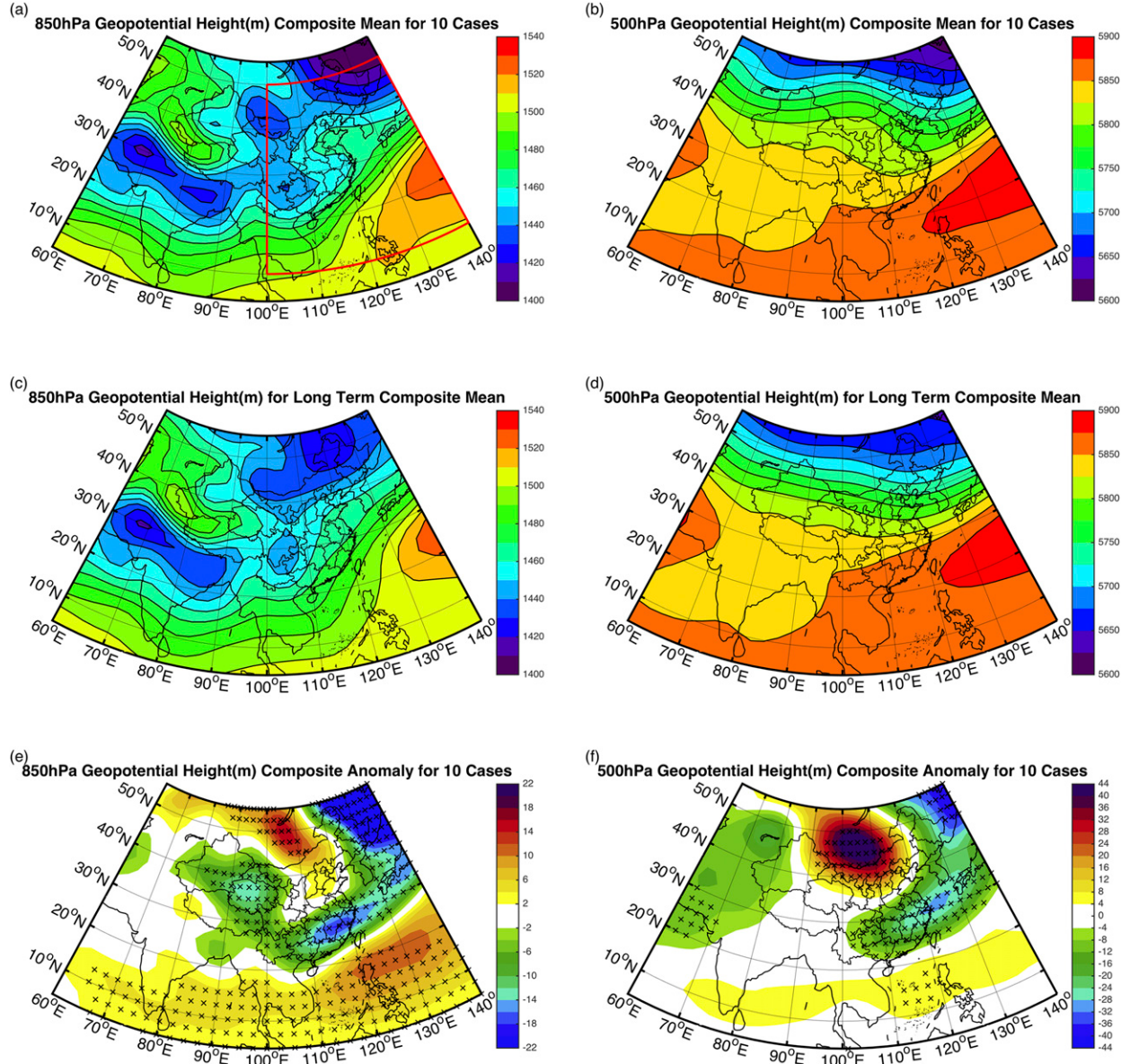


FIG. 3. (a) The 850-hPa composite mean geopotential height for the 10 cases. (b) As in (a), but for 500 hPa. (c) The 850-hPa long-term composite mean geopotential height for the 10 cases. (d) As in (c), but for 500 hPa. (e) Departures from the 30-yr daily long-term-mean climatology for the 10 cases in 850 hPa. (f) As in (e), but for 500 hPa. The red rectangle in (a) is the area for calculating spatial correlation. The \times dots in (e),(f) indicate points that passed the significance test.

the same day with the maximum TP surface temperature anomaly.

The composite means of NCEP 850- and 500-hPa geopotential height for the 10 PEPEs' period were shown in Figs. 3a and 3b, revealing a typical mei-yu circulation pattern. The west Pacific subtropical high extended from southern Japan to southeast China with a dominant southwesterly flow in southern China in the lower troposphere. In midlatitude, a blocking high lies at around 105°E , transporting cold air to the southeast and

meeting the warm and wet air from the southwesterly flow from south at the Yangtze Plain and causing the persistent precipitation there (Ding 1992; Ding and Chan 2005). With some triggers such as shear lines or vortex in the lower layer, precipitation will occur in the Yangtze Plain. However, as shown in Figs. 3e and 3f, different from a typical mei-yu case, there is an enhanced west Pacific subtropical high featured with increasing lower-level monsoon jet flow at the 850-hPa level. At the 500-hPa level, there is a significant

TABLE 2. Spatial correlation coefficient of 850-hPa geopotential height and their *p* value for the significance test. Boldface values indicate those that passed the significance test.

Year	Start date	End date	Original		Anomaly to climatology	
			Coef	<i>p</i> value	Coef	<i>p</i> value
1992	4 Jul	8 Jul	0.75	0.593	0.91	0.038
1994	13 Jun	17 Jun	0.83	0.465	0.76	0.229
1997	2 Jul	9 Jul	0.92	0.183	0.79	0.183
2000	9 Jun	12 Jun	0.74	0.608	0.85	0.126
2000	17 Jul	22 Jul	0.90	0.259	0.67	0.373
2002	14 Jun	17 Jun	0.95	0.065	0.87	0.076
2005	18 Jun	24 Jun	0.95	0.042	0.80	0.176
2006	4 Jun	7 Jun	0.89	0.299	0.59	0.513
2008	7 Jul	12 Jul	0.85	0.426	0.55	0.579
2010	17 Jun	25 Jun	0.95	0.078	0.90	0.041

strengthened blocking high system to the north of the mei-yu regions. Both anomalous systems (west Pacific subtropical high and the blocking high) induce the stable anomalous circulations that result in the severe persistent precipitation. Long-term composite mean for the 10 cases were also derived by the NCEP 1981–2010 long-term daily mean data and are shown in Figs. 3c and 3d. An obvious difference between Figs. 3a and 3c is that the ridge around 30°–40°N, 110°–130°E at the east of the TP in 850 hPa extends much farther northward during the PEPEs periods than that in the 1981–2010 climatology. A low center can be found in Sichuan basin (25°–35°N, 100°–110°E) in both 10 cases' composite mean and long-term composite mean geopotential height field in the 850-hPa layer. A deeper trough around 120°–130°E, and a higher ridge around 100°–110°E can be found in the 500-hPa layer during the PEPEs periods by comparing Figs. 3b and 3d. Anomalies through the 10 events defined as departures from the 1981–2010 daily long-term means for the days were presented in Figs. 3e and 3f. Bootstrap (Mooney and Duval 1993; Wilks 2006, 166–170), a random resample nonparametric statistical test, was employed here to assess whether the anomaly is significant. We randomly chose 1000 consecutive 5 days from June to August 1991–2010 as the sample pool, then randomly selected 10 periods from the 1000 samples and calculated their composite mean. Then we repeated this resample process 1000 times to obtain an ensemble. If the 10-case anomaly was not significant, the 10 PEPEs' composite mean should obey the same distribution of the resample outputs. After deriving the anomaly geopotential height for the 1000 resample outputs, we get the 90% confidence interval for the mean anomaly. We set the significance test level at $\alpha = 0.1$. Grids with the 10 PEPEs' composite mean geopotential height anomaly outside the 90% confidence interval were regarded as having a significant difference to the long-term mean. Points that passed the significance test were marked with a crisscross

(\times) in Figs. 3e and 3f. A significant low anomaly can be found in southern China and a high anomaly can be found in northern China at 850 hPa. This pattern is more obvious and significant at 500 hPa. The stations under the low pressure anomaly experienced PEPE during the 10 cases in southeastern China. A low pressure anomaly generates convergence and the uplift of air mass and convection most likely initiates in a low pressure center. On the other hand, the high pressure anomaly in northern China blocks the northward movement of the low pressure system. The longer the low pressure system is sustained, the more persistent is the precipitation event.

To select a typical case for a detailed numerical modeling study, we calculated the spatial correlation coefficient between the 850-hPa geopotential height of the 10 cases and the 10 cases' composite mean for a domain within 10°–50°N, 100°–140°W (red rectangle in Fig. 3a). Results are listed in Table 2. Half of those cases' correlation coefficients were greater than 0.9. A bootstrapping test was employed to assess whether this correlation is significant. We randomly selected 1000 consecutive 5 days from June to August 1991–2010 as resamples and calculated the correlation coefficients of those cases. Histogram results are shown in Fig. 4a, and most of the random cases' correlation coefficients were greater than 0.8. The probability value (*p* value) for each case was obtained by dividing the number of sample with its greater correlation coefficients than the selected one by 1000. Even though several PEPE cases passed the significant test with *p* value less than 0.1, the climatic pattern needs to be removed to ensure a more convincing result. We set the 30-yr long-term summer-mean geopotential height as the climatic pattern. For all the 10 cases' composite mean, each PEPE case, and each random case, we subtract the 30-yr long-term summer mean before calculating the correlation coefficient. New results are shown in Fig. 4b and outputs are listed in Table 2. The correlation coefficients of the 1000 random cases decrease rapidly; however, most of the

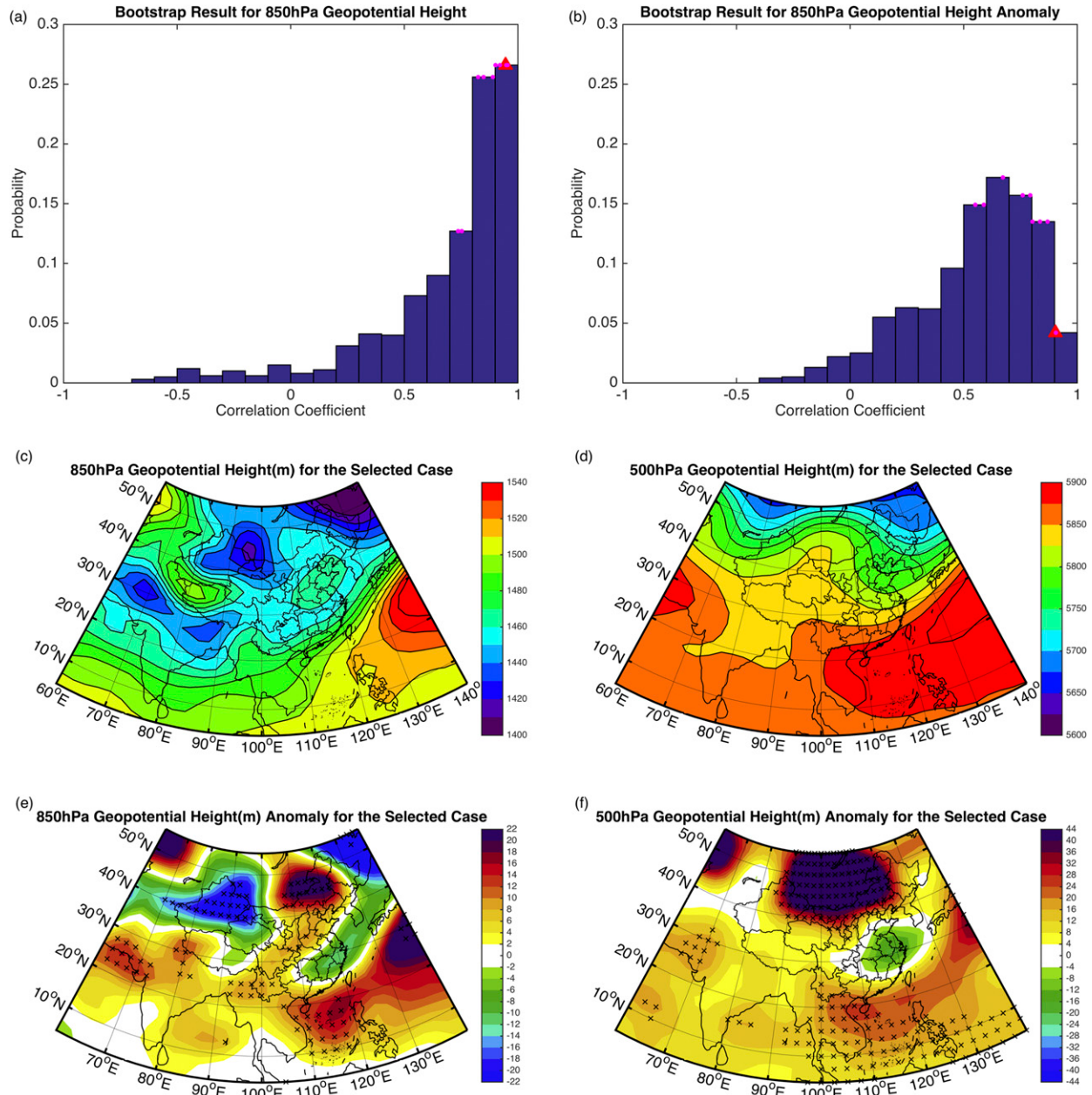


FIG. 4. (a) Statistical results of the correlation coefficients to long-term composite mean. Bars are the statistical results of the 1000 random cases. Magenta dots are the results of the 10 cases. The red triangle is the result of the select case (17–25 Jun 2010). (b) As in (a), but for the anomaly to 1981–2010 summer long-term mean. (c) 850-hPa geopotential height for the select case. (d) As in (c), but for 500 hPa. (e) 850-hPa geopotential height anomaly to long-term composite mean. (f) As in (e), but for 500 hPa. The \times dots in (e),(f) indicate points that passed the significance test.

10 cases still maintain a very high correlation coefficient. Only cases that happened in 2002 and 2010 passed both significant tests. Based on those tests of statistical significance, we selected the case that happened from 17 to 25 June 2010 for further study.

This selected case has a high correlation coefficient (0.90) and low p value ($p < 0.05$). It also has the longest

episode and maximum precipitation among the 10 cases. Five stations (red triangles in Fig. 1) experienced station PEPE during this precipitation event with the maximum precipitation of 754.40 mm. Daily precipitation during this period from station observation is shown in Fig. 5a.

The geopotential height field of this case and its anomaly to long-term composite mean in 850 and

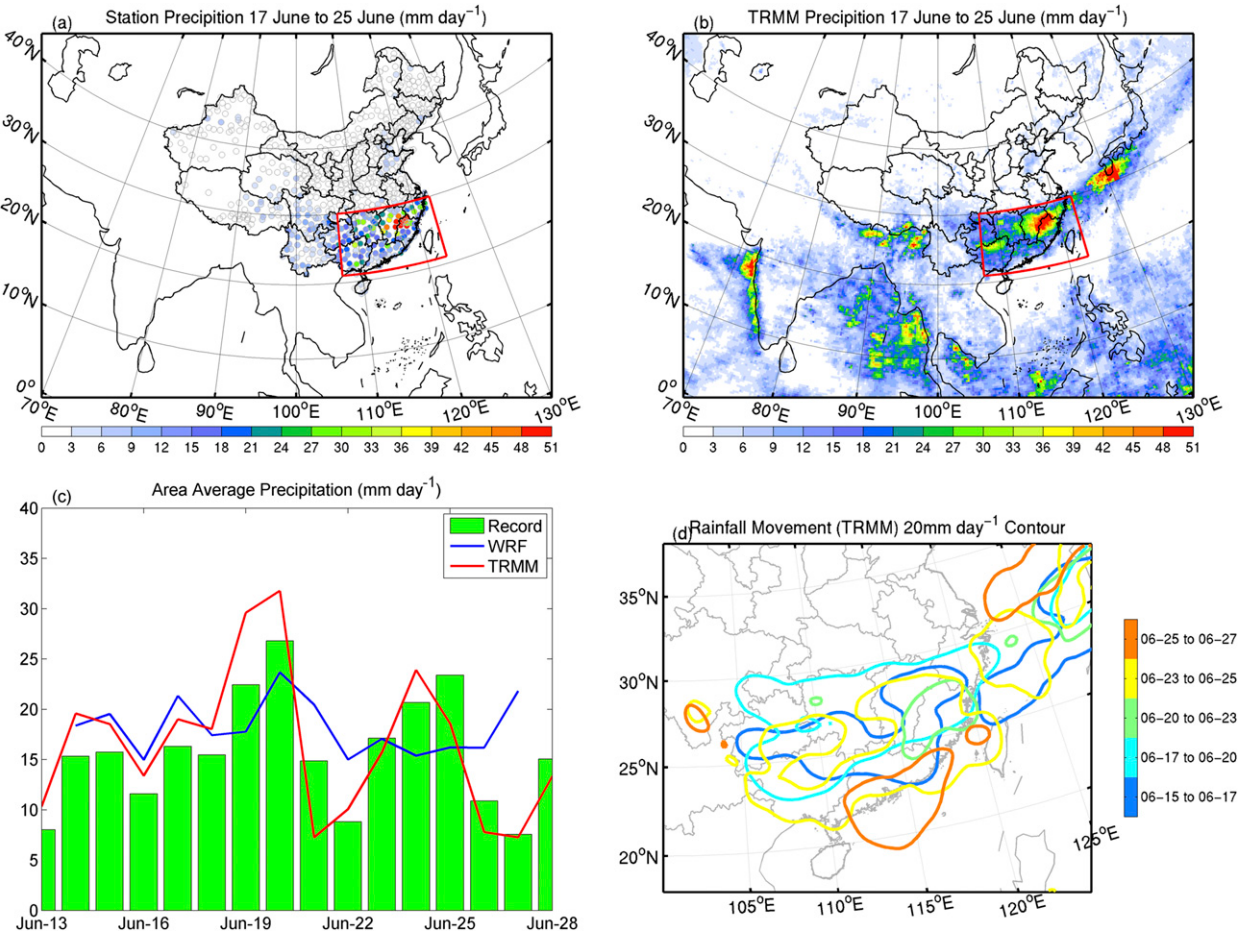


FIG. 5. (a) The daily station precipitation averaged for the study period. (b) As in (a), but for the TRMM precipitation. (c) Time series of area-averaged rainfall in the red rectangle over land points only. The green bars are daily resolutions of station observations. The red line shows 3-hourly resolutions of the TRMM dataset. The blue line shows hourly WRF CNTL results. (d) TRMM rain area movement: different colors represent different time periods.

500 hPa are shown in Figs. 4c–f. The geopotential height field of this case was similar to the composite mean. A high pressure center can be found around 30°–40°N, 110°–130°E at 850 hPa that corresponds to the ridge in the composite mean field. The trough and ridge at 500 hPa were almost at the same position as those in the 10 cases' composite mean. Anomaly analyses indicate a significant high pressure anomaly in northern China at both 850 and 500 hPa. By comparing Figs. 4e, 4f, and 5a, we found that the maximum rainfall is nearly at the center of the low pressure anomaly at 850 hPa.

4. Numerical model experiments

The selected PEPE starts at 2000 China standard time (UTC + 8 h) 16 June 2010. According to Fig. 2, the TP surface air temperature is anomalously high about 3–4 days before the PEPE onsets, so the model

simulations started at 0000 UTC 13 June, 3.5 days prior to the onset of the PEPE, allowing 3.5 days for the model to spin up.

Our simulations used the WRF-ARW version 3.6 (hereinafter WRF) with a single 280×180 horizontal domain (Fig. 1) centered at 30°N, 120°E, with 30-km horizontal grid spacing and 51 vertical levels. The WRF physics schemes used here includes the RRTM for GCMs (RRTMG) longwave and shortwave radiation scheme (Iacono et al. 2008), the Noah-MP land surface scheme (Niu and Yang 2004; Niu et al. 2011; Yang et al. 2011; Barlage et al. 2015), the YSU boundary layer scheme (Hong et al. 2006), the WRF single-moment (WSM) 6-class graupel microphysical scheme (Hong and Lim 2006), and the Grell–Freitas ensemble cumulus scheme (Grell and Freitas 2014). FNL data were used to generate the lateral boundary and initial conditions for WRF. The sea surface temperature from FNL was updated every 6 h.

Land state variables such as soil temperature and soil moisture play an important role in land surface processes. Since this paper focuses on the impact of land surface processes on precipitant events, accurate initial soil condition are required to capture the evolution of surface sensible and latent heat fluxes. We employed HRLDAS (Chen et al. 2007), an offline land data assimilation system for generating WRF land system consistent soil conditions, along with the Noah-MP land surface model in this study. Atmosphere forcing data such as downward shortwave and longwave radiation, surface pressure, wind speed, temperature, humidity, and precipitation were taken from the 3-hourly 0.25° global land data assimilation system land surface dataset. Normally, it took about 17 months to obtain equilibrium soil condition by HRLDAS (Chen et al. 2007). However, due to complex terrain of the Tibetan Plateau and surround areas as well as the more complex Noah-MP land model, it took about 5 years for HRLDAS to spin up in our study (Gao et al. 2015; Zhang et al. 2016). The soil moisture, soil temperature, snow water equivalent, and canopy water from the spunup output of HRLDAS were used as the initial WRF soil condition input.

To investigate the impact of the Tibetan Plateau's surface heating on the evolution of the extreme-precipitation episode discussed above, three WRF experiments were designed with contrasting soil moisture conditions. It is not desirable to break surface energy balance by arbitrarily setting surface heating conditions, so WRF experiments were designed by changing initial soil moisture conditions that would subsequently affect the surface heating but still maintain a consistent surface energy budget throughout model simulations. The land surface energy budget contains seven main components as seen in Eq. (1) below, where SW_{\downarrow} is the downward shortwave radiation, LW_{\downarrow} and LW_{\uparrow} are the downward and upward longwave radiation, α is albedo, SH_{\uparrow} is sensible heat flux, LH_{\uparrow} is latent heat flux, and Rg_{\downarrow} is ground heat flux transferred into soil:

$$SW_{\downarrow} + LW_{\downarrow} = SW_{\downarrow} \times (1 - \alpha) + LW_{\uparrow} + SH_{\uparrow} + LH_{\uparrow} + Rg_{\downarrow} \quad (1)$$

The sensible heat flux directly provides heating to the PBL; the stronger the sensible heat flux, the warmer the PBL. The latent heat flux, however, provides sources of water vapor to the PBL. In this WRF sensitivity study, our primary objective was to control the partition of incoming energy into latent heat fluxes and sensible heat fluxes, so the surface heating in the TP can be maximized or minimized. In Noah-MP, each type of soil texture has a wilting point and a saturation point. The wilting point means the critical point that soil ceases

evaporation, and the saturation point means when the soil moisture reaches its maximum (Noilhan and Planton 1989). The values of these soil parameters are specified in a table (<http://www.ral.ucar.edu/research/land/technology/noahmp/HRLDAS-v3.6/SOILPARM.TBL>) in WRF as a function of soil texture. The latent heat fluxes are reduced to the minimum by setting the initial soil moisture in all four layers to the wilting point that corresponds to a specific soil texture for a given WRF grid point, and similarly increased to its maximum by using saturated soil moisture. As a result, three WRF numerical experiments were conducted with contrasting scenarios of soil moisture variations over the TP: 1) a control case (hereafter CNTL), using the well spunup soil moisture fields obtained from HRLDAS as initial conditions; 2) a dry case (hereafter DRY), setting the initial four-layer WRF soil moisture to the wilting point so that evaporation ceases; and 3) a wet case (hereafter WET), in which the initial four-layer WRF soil moisture was set to the saturation values according to each specified soil texture.

5. Results and discussion

We applied station observations and TRMM data to analyze the evolution and movement of extreme precipitation. Figures 5a and 5b show the station and TRMM daily precipitation averaged for this study period, which agree with each other well in the distribution and intensity of the precipitation. The TRMM even captured some scatter precipitation events very well. Figure 5c compares the time series of land-point daily precipitation from stations, TRMM and the control WRF simulation (CNTL) in the red rectangle. All three datasets were synchronized to China standard time and averaged to a daily interval. The CNTL simulation depicted the observed rainfall pattern well in the first week, but as the simulation progressed in time, errors accumulated and it did not compare well with observations after 21 June. However, it captured the main area of heavy rain very well. While station daily precipitation measurements are scattered, TRMM's higher temporal and spatial resolution provides better information about the evolution of PEPEs. Moreover TRMM agrees well with station observations in total precipitation (Figs. 5a and 5b). Therefore, the gridded TRMM dataset is used here for analyzing the movement of the precipitation system.

Figure 5d shows the propagation of the precipitation system based on the TRMM data. Different colors represent different time periods. All lines are contours at the value of 20 mm day^{-1} . We applied cowbell spatial filtering described by Barnes et al. (1996) to process data due to the scattering nature of summer convective precipitation. This PEPE started from $20^{\circ}\text{--}30^{\circ}\text{N}$, $105^{\circ}\text{--}120^{\circ}\text{W}$

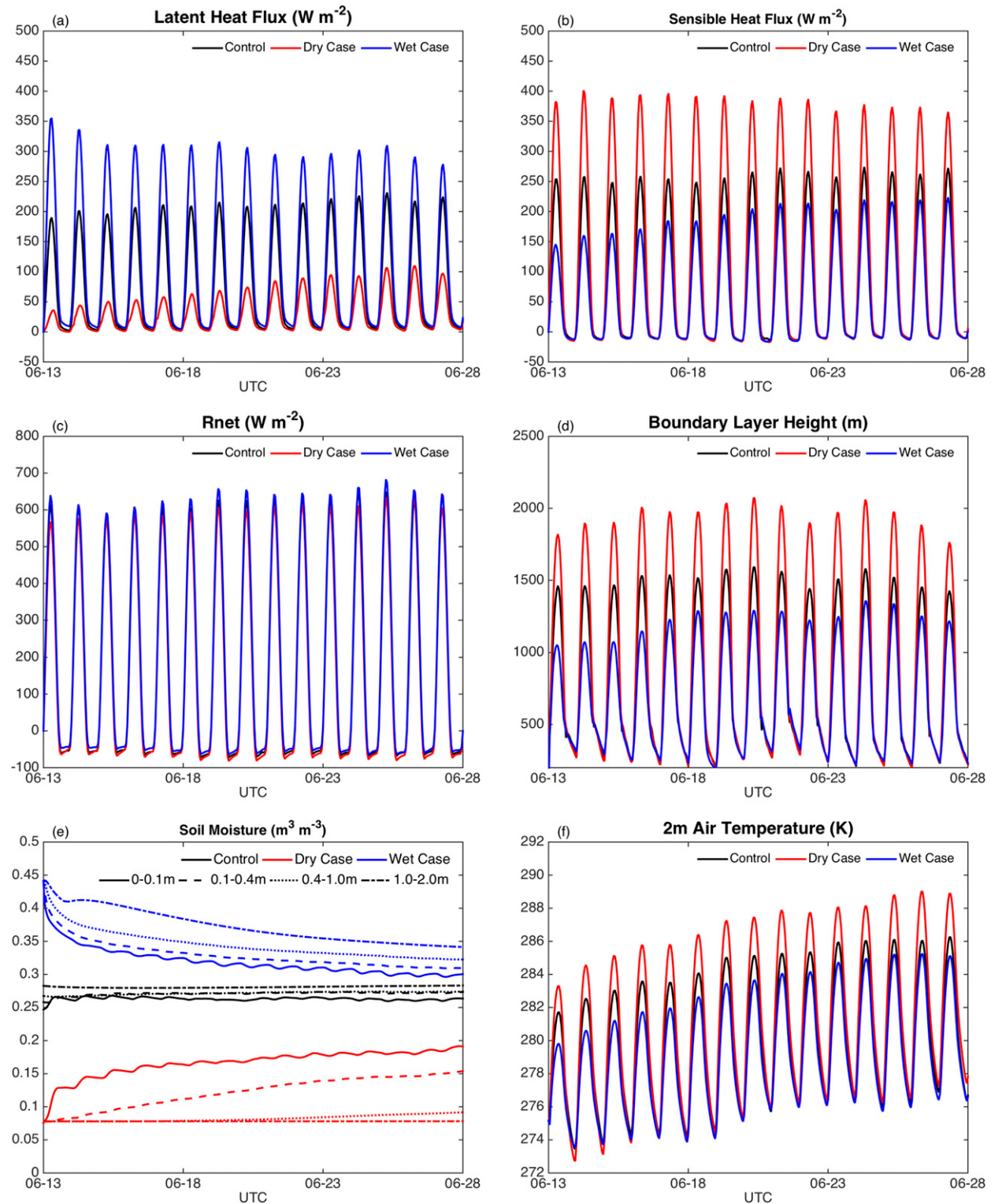


FIG. 6. The average land surface and soil elements over the Tibetan Plateau: (a) latent heat flux, (b) sensible heat flux, (c) net downward radiation, (d) boundary layer height, (e) soil moisture for four layers (different line types for different layers and different colors for different cases), and (f) 2-m air temperature.

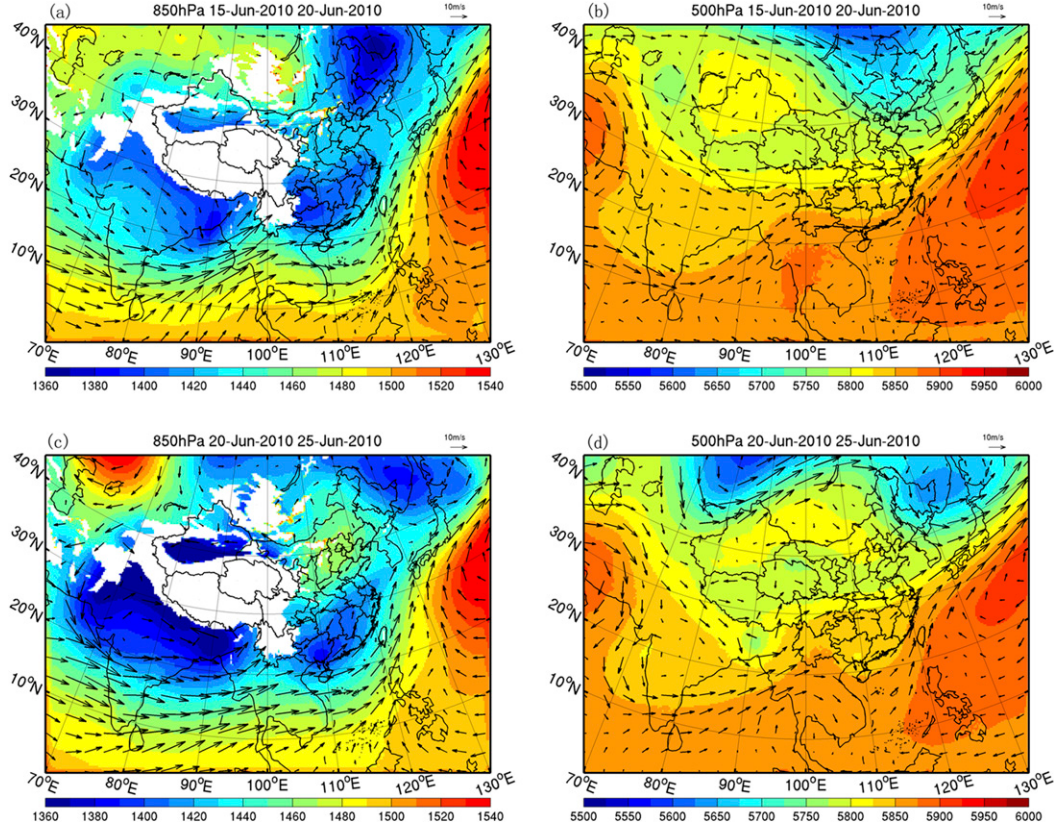


FIG. 7. (a) Time-average 850-hPa geopotential height field, wind speed, and direction of CNTL output during 15–20 Jun. (b) As in (a), but for 500 hPa. (c) As in (a), but for 20–25 Jun. (d) As in (c), but for 500 hPa. Vectors are for wind speed.

and continued at 25°–30°N, 110°–120°W for about 10 days, during 15–25 June. The rain concentrated at 25°–30°N, 112°–120°W during 20–23 June, the same area also having the most intense rainfall during the entire raining period. After 25 June, the rain dissipated in southern China and moved northeast. At the same time, another precipitation occurred in the South China Sea. Even though the PEPE (precipitation exceeded 50 mm day⁻¹) onset occurred on 17 June according to station observations, our further analysis was conducted from 15 June when the heavy rain spread in this region.

As shown in Fig. 6, setting the soil moisture to its wilting point at TP in DRY reduced significantly latent heat fluxes (Fig. 6a). However, the net radiation of DRY and WET cases was nearly the same as CNTL (Fig. 6c) where energy was transferred to the atmosphere by sensible heat flux, resulting in much higher sensible heat fluxes (Fig. 6b). Higher sensible heat fluxes, in turn, promote stronger turbulence and produce stronger thermals, and deeper and more vigorous vertical mixing in the planetary boundary layer (Fig. 6d). Many studies showed that soil moisture has a long memory (Koster and Suarez 2001; Wu

and Dickinson 2004). Even spring's soil moisture can impact summer's land surface process (Wang et al. 2014). In our simulation, the soil moisture did restore (Fig. 6e) faster in the upper layer than the deeper layer in both DRY and WET cases. But even at the end of our simulation, the WET simulation still has the highest soil moisture in all soil layers and the DRY case has the lowest soil moisture. Along with the decreasing difference of soil moisture among three simulations, the difference of sensible heat flux was also reduced. But the increase/decrease in sensible heat fluxes persisted to the end of our simulation even though only the initial soil moisture was changed. Higher sensible heat fluxes in DRY resulted in higher 2-m air temperature. The 2-m air temperature in the DRY case was about 1°–2°C higher than that in CNTL, a signal similar to the temperature warm anomaly over the TP prior to PEPEs.

a. WRF control simulation

Figure 7 shows the 850- and 500-hPa geopotential height field and wind speed of CNTL. Figures 7a and 7b are for 15–20 June and Figs. 7c and 7d are for 20–25 June. The precipitation had already started by 15 June. In the

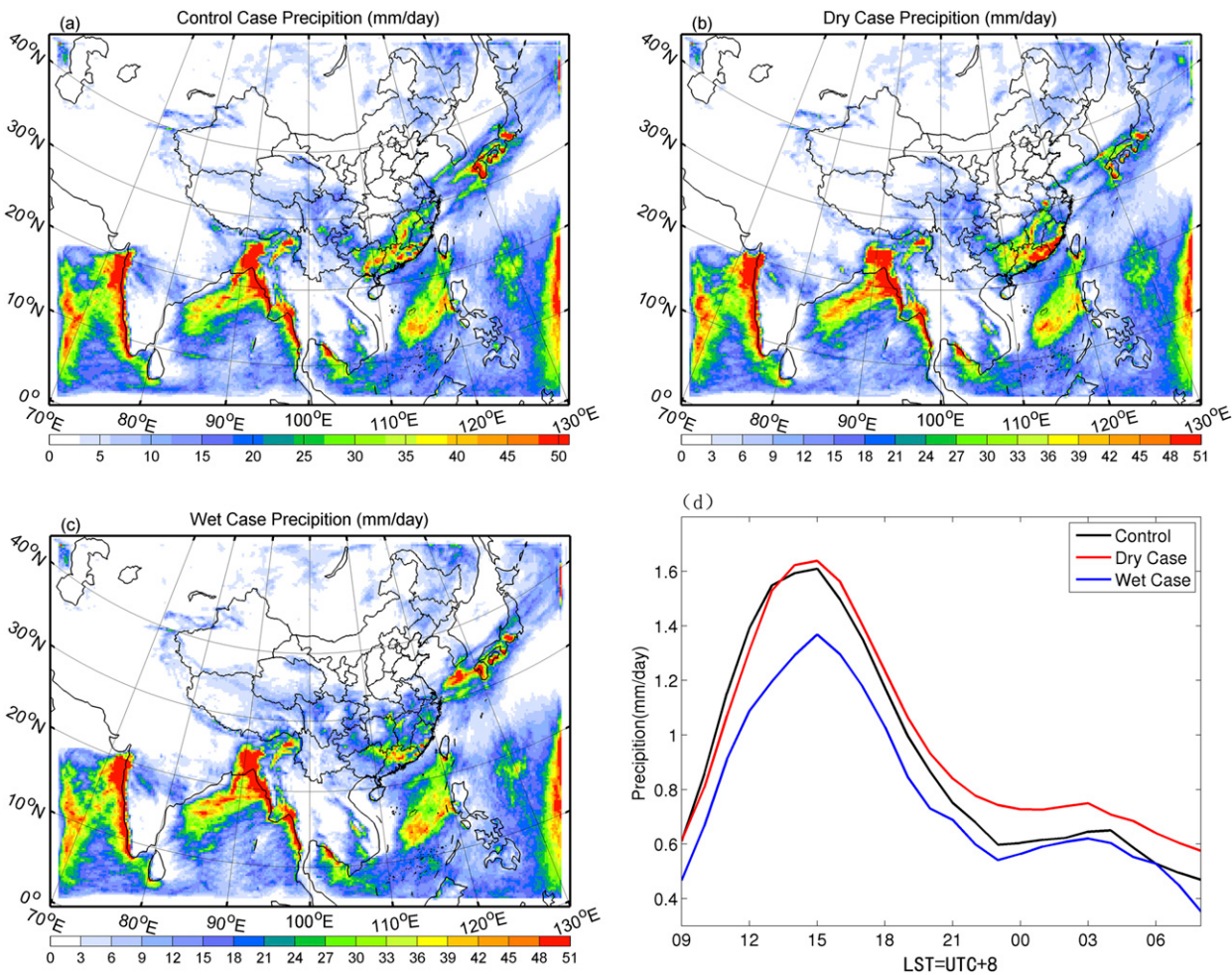


FIG. 8. Daily rainfall in (a) CNTL, (b) DRY, and (c) WET. (d) Diurnal cycle of the mean precipitation intensity in the red rectangle in Fig. 1.

850-hPa layer, southern China was dominated by a low pressure system for the whole 10 days (15–25 June). A high pressure belt splits the southern China low pressure and the deep trough existed in northeast China during the first 5 days. The high pressure belt developed into a high center during the last 5 days, and the high precipitation center coincides with its position in the NCEP reanalysis data (Fig. 4c). A 500-hPa subtropical high was the dominant feature over the west Pacific Ocean. The ridge over Mongolia enhanced greatly during the last 5 days, agreeing with the development of the high pressure center at 850 hPa. In general, the WRF simulations did capture well the synoptic pattern of this case and the high pressure in the north of the rain belt, which is the main common feature of the 10 PEPEs.

The WRF CNTL area-averaged precipitation (for domain in the red rectangle in Fig. 1) is shown in Fig. 5c. It agrees well with station observations and TRMM in the first week, but errors accumulated in the second

week. Also, in order to determine the TP's impact on the Bay of Bengal, the modeling domain was designed to be much bigger than our focus area to minimize the impact of lateral boundary conditions, which may cause some drift in synoptic systems simulated in WRF. Even though it is expected that the area-averaged precipitation does not agree with the observation very well in the late stages of simulation, the time-averaged precipitation in CNTL well captured the location and intensity of the extreme precipitation over land in southern China (Fig. 8a). The precipitation center in southern China was slightly placed more northward in the control simulation but the total precipitation area was close to TRMM. The location and intensity of precipitation in Japan agrees with the TRMM very well, and most precipitation happened in the southern part of Japan. However, the model overestimated the precipitation over oceans, especially in the South China Sea, the Bay of Bengal, and west of India.

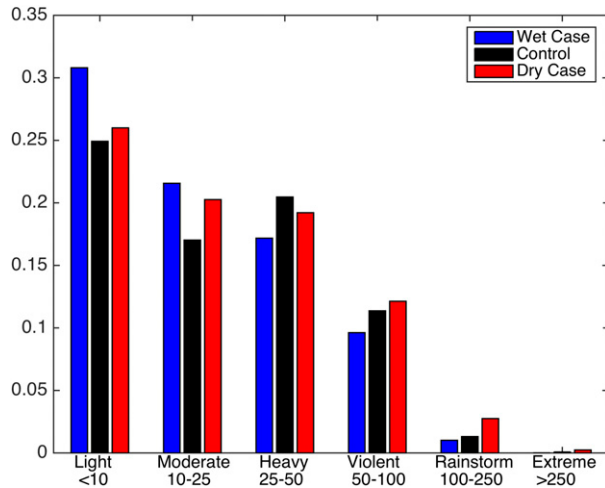


FIG. 9. Precipitation probability of different rain categories for 15–25 Jun in the red rectangle in Fig. 1.

b. Precipitation pattern simulated in WRF sensitivity simulations

The temporally averaged precipitation from the three WRF sensitivity experiments is shown in Figs. 8a–c. The DRY simulation has the highest precipitation amount over southeastern China, while the WET simulation produces the lowest rainfall among the three simulations, which is consistent with the analysis of observations presented in section 2: a warmer TP surface usually resulted in PEPE in southern China. However, things were different over Japan. The DRY case has the lowest precipitation in Japan. The diurnal cycle of precipitation is shown in Fig. 8d. The DRY case is most notably different from CNTL in nighttime precipitation. Note that the precipitation is typically at its minimum at nighttime. The WET case has lower precipitation during daytime while it has similar precipitation to the CNTL during nighttime. This difference in the diurnal cycle of precipitation between DRY and WET in relation with water vapor transport is further discussed in section 5d.

Not only has the total precipitation amount changed, the intensity of the precipitation was also modified. Figure 9 shows the daily rainfall probability of different categories over the land in the red rectangle in Fig. 1 during 15–25 June. The threshold values of different precipitation categories (from light to extreme) are based on definitions from the China Meteorological Administration. The WET simulation is dominated with “light” to “moderate” precipitation categories (less than 25 mm day^{-1}), while the DRY simulation features more “violent,” “rainstorm,” and “extreme” categories (with precipitation greater than 50 mm day^{-1}). The CNTL simulation seems to be in the middle of WET and DRY with more “heavy” precipitation ($25\text{--}50 \text{ mm day}^{-1}$). It is

clear that drier (wetter) the TP surface is, the more (less) extreme the precipitation would be.

Based on the above analysis, we further split the precipitation amount into three categories: less than 25 mm day^{-1} , $25\text{--}50 \text{ mm day}^{-1}$, and greater than 50 mm day^{-1} , which represent the dominating rainfall categories in WET, CNTL, and DRY simulations, respectively. We analyzed the areas of the different rainfall categories’ by averaging the corresponding daily rainfall intensity, respectively (i.e., for light precipitation, we only chose days with less than 25-mm rainfall and calculate the temporal average). The results are shown in Fig. 10. The areas corresponding to the three rainfall categories differ greatly in three simulations. Obviously precipitation events with greater than 50 mm day^{-1} contribute most to the total precipitation even though it has the lowest probability of occurrence. Clearly, the DRY simulation has the most “extreme rainfall” events and the WET simulation had the most “light rain” events. This corresponds to each case’s precipitation intensity frequency. In the top row, for light rain ($0\text{--}25 \text{ mm day}^{-1}$), the WET case has the most precipitation and the highest frequency of light and moderate precipitation (Fig. 9). The middle and bottom row have the same feature. The CNTL case has the most “heavy rain” and the bottom row has the most “extreme rain,” which is the same as the frequency feature in Fig. 9. It seems that a wet TP surface facilitates the “light rainfall,” but a dry TP surface inhibits it.

c. Tibetan surface heating and PBL structures

Different soil moisture leads to different surface heating, and strong surface heating will promote stronger turbulence and a deeper planetary boundary layer. As discussed above, the DRY simulation leads to a warmer and deeper boundary layer. To determine the surface heating’s impact on atmosphere circulations, it is necessary to examine PBL features over the TP and its surrounding areas. As shown in Fig. 11, the air in the PBL in DRY was warmer and the air atop the PBL is colder than that in CNTL, consistent with stronger vertical mixing in DRY relative to CNTL. A warmer and deeper PBL implies lower pressure at the bottom of the layer and higher pressure above the top of the layer. As such, air converged in the lower layer and diverged above the PBL. A high pressure and cold air mass was generated between 6000 and 8000 m above sea level. The eastward wind jet, even though reduced by the high pressure above the Tibetan Plateau, still controlled the average wind speed. Since pressure at a given level is determined by the whole air mass above that level, the surface pressure is determined by the total air mass above the surface. Because of its higher density, a layer

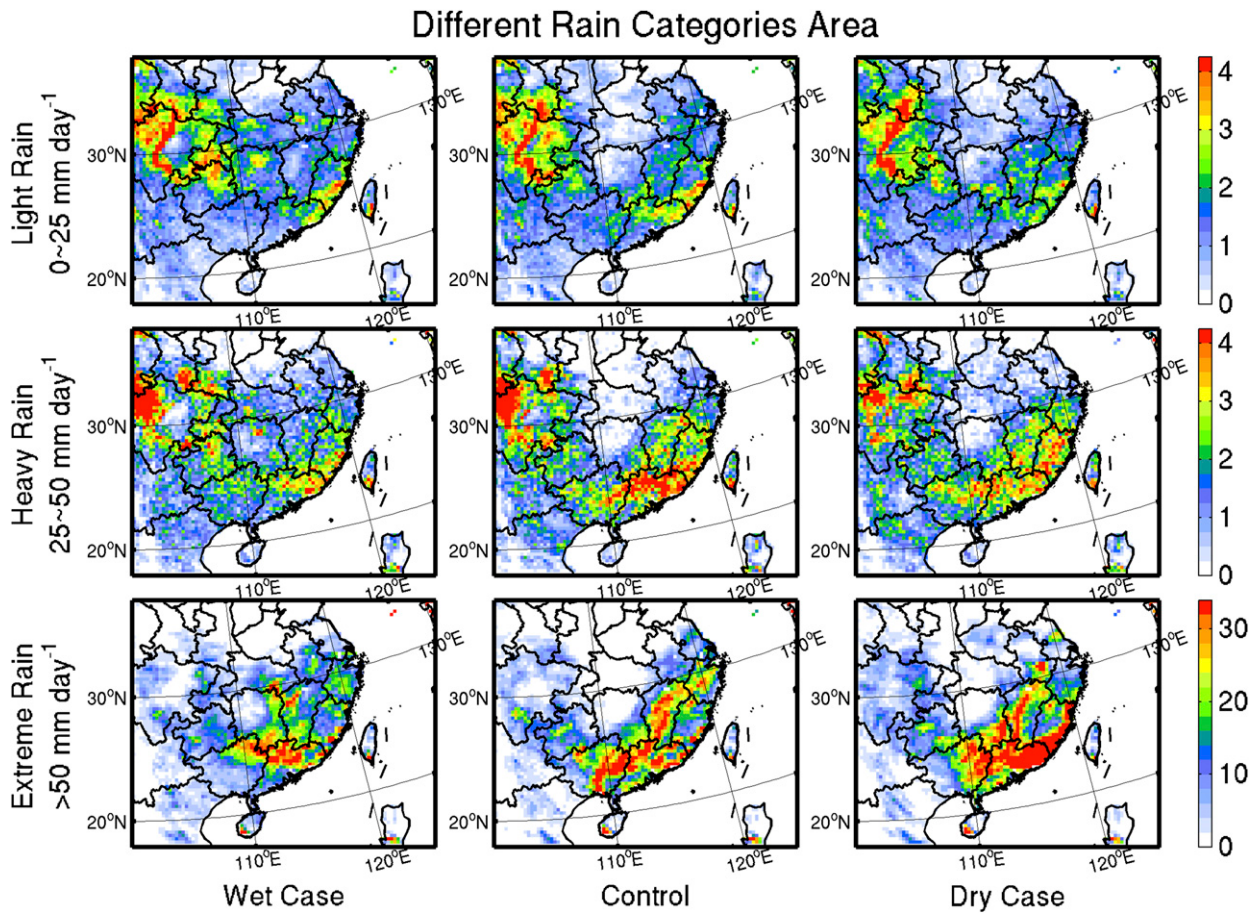


FIG. 10. (top) Precipitation intensity (mm day^{-1} , shown in the side bar) averaged for 15–25 Jun from light rain events ($0\text{--}25 \text{ mm day}^{-1}$) for each given WRF grid. (middle) As in (top), but from heavy rain ($25\text{--}50 \text{ mm day}^{-1}$). (bottom) As in (top), but from extreme rain ($>50 \text{ mm day}^{-1}$). (from left to right) WET, CNTL, and DRY. Note that the side bar for the bottom row ($0\text{--}34 \text{ mm day}^{-1}$) differs from the first two rows.

of cold air mass was heavier and produced a higher pressure under it, which was then transported downstream along with the cold air mass. As shown in Figs. 11b and 11c, the top of the high pressure air mass in Fig. 10c coincided with the top of the cold air mass in Fig. 11b. The warm air descended from the TP surface to the Sichuan basin, compensating for the preexisting cold air between 17 and 19 June, which created a new low pressure in the Sichuan basin during this period. In conclusion, the strong heating at the Tibetan surface can generate a high pressure system downstream.

d. High pressure anomaly downstream of the TP

When moving eastward, the aforementioned high pressure merged with the preexisting high pressure system over the Yangtze Plain. As shown in Fig. 12, the preexisting high pressure was further enhanced in the DRY simulation, especially at the 700-hPa level that is lower in altitude than the TP surface. The difference at

the 500-hPa level was almost the same as the difference at 700 hPa but a bit northerly. At 300 hPa, the high anomaly at the north of the rain belt was almost gone and located even more north than 500 hPa. There is no clear high pressure center around $35^{\circ}\text{--}45^{\circ}\text{N}$, $100^{\circ}\text{--}130^{\circ}\text{E}$, but there is a clear positive difference over the Tibetan Plateau. This is consistent with Fig. 11c because 300 hPa corresponds to about 9-km altitude in a standard atmosphere. In Fig. 11c, the main pressure anomaly downstream was under 8 km and above 9 km. Hence, 300 hPa was approximately the upper limit of the TP's surface heating impact altitude downstream. Over the Tibetan Plateau, the stronger surface sensible heating induces the strengthened thermal effects of the Tibetan Plateau, then generates the anticyclone anomaly in the upper troposphere, which induces an upper-level Rossby wave train, and propagates eastward along with the upper-level easterly jet flow. In the lower troposphere, the thermal effect of the TP induces a cyclonic

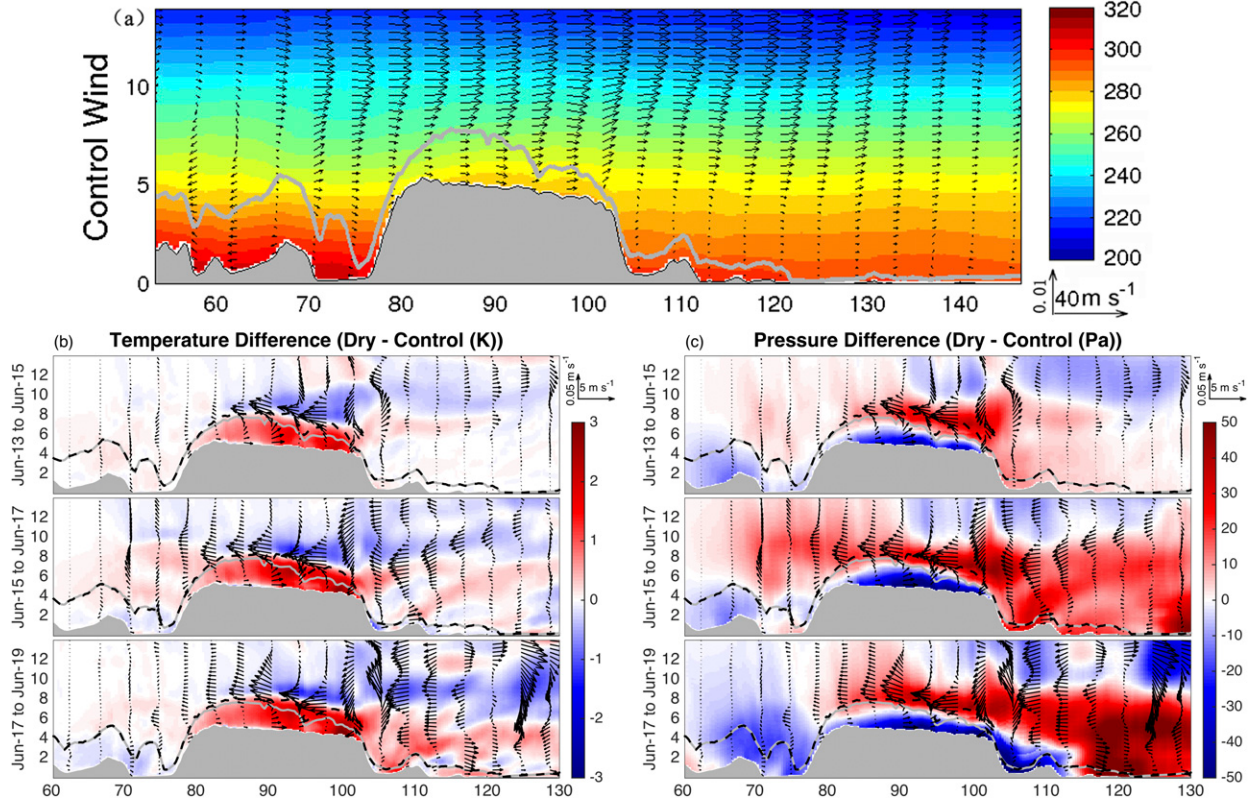


FIG. 11. (a) Cross section along the transect AB of Fig. 1 with latitudinal-averaged values from 30° to 35°N and temporal-averaged values from 15 to 25 Jun. The gray shading indicates the terrain, the gray line shows the daily average boundary layer height, colors show the temperature (K), and vectors are for the longitudinal and vertical wind. (b) Temperature differences (in K) between DRY and CNTL. The black dashed line indicates the DRY simulation's noontime [1000–1400 local time (UTC + 6 h)] PBL height and the gray line is the CNTL simulation's PBL height. Vectors are for the longitudinal and vertical wind difference. (c) As in (b), but for pressure differences (in Pa).

anomaly that enhances the low-level monsoon jet flow along with the intensification of west Pacific subtropical high in southern China (Bao et al. 2010; Wang et al. 2008). The 200-hPa geopotential height difference was similar but more significant to 300 hPa.

As discussed above, the PEPE concentrated in southern China mainly because the high pressure system blocked the northward movement of the low pressure system, and hence formed favorable circulations for heavy precipitation (a strong TP surface heating helps enhance the high pressure). Such a high pressure anomaly hinders the northward movement of the low pressure center in southern China, and keeps it sustained in southern China for a longer duration. To show the movement of the low pressure center, the contours of the 1410-m line at 850 hPa and the 5820-m line at 500 hPa for different time period are combined in one figure. The contour lines of 1410 m at 850 hPa approximately represent the boundary of the low pressure center in Figs. 7a and 7c. Figure 13 shows the movement of the 1410-m contour lines at 850 hPa and that of the 5820-m line at 500 hPa. Different colors mean different

time periods as in Fig. 5d. In 850 hPa, the low pressure center was located at almost the same position in all the three WRF simulations during 15–17 June (the blue line in the left panel in Fig. 13). However, as time progresses, the low pressure system's position differs significantly. After 23 June, the low pressure system already reached Korea in the WET simulation and approached Korea in the CNTL simulation (the yellow line). The low pressure system WET was located farther north than that in CNTL after 23 June. However, in the DRY simulation, the low pressure system still remained in southern China, where the contour line was still located in the mainland and has not reached the sea. It is even more obvious after 25 June. The contour line already passed Korea in WET, and approached Korea in CNTL (the pale brown line). But in DRY, the contour line remained in the mainland of China. This again confirms that the high anomaly did effectively hinder the northward movement of the low pressure system. The 500-hPa contour lines show a similar pattern in the right panel of Fig. 13. They started at the same position in 15 June (blue line). The contour lines of CNTL and WET cases were almost identical but

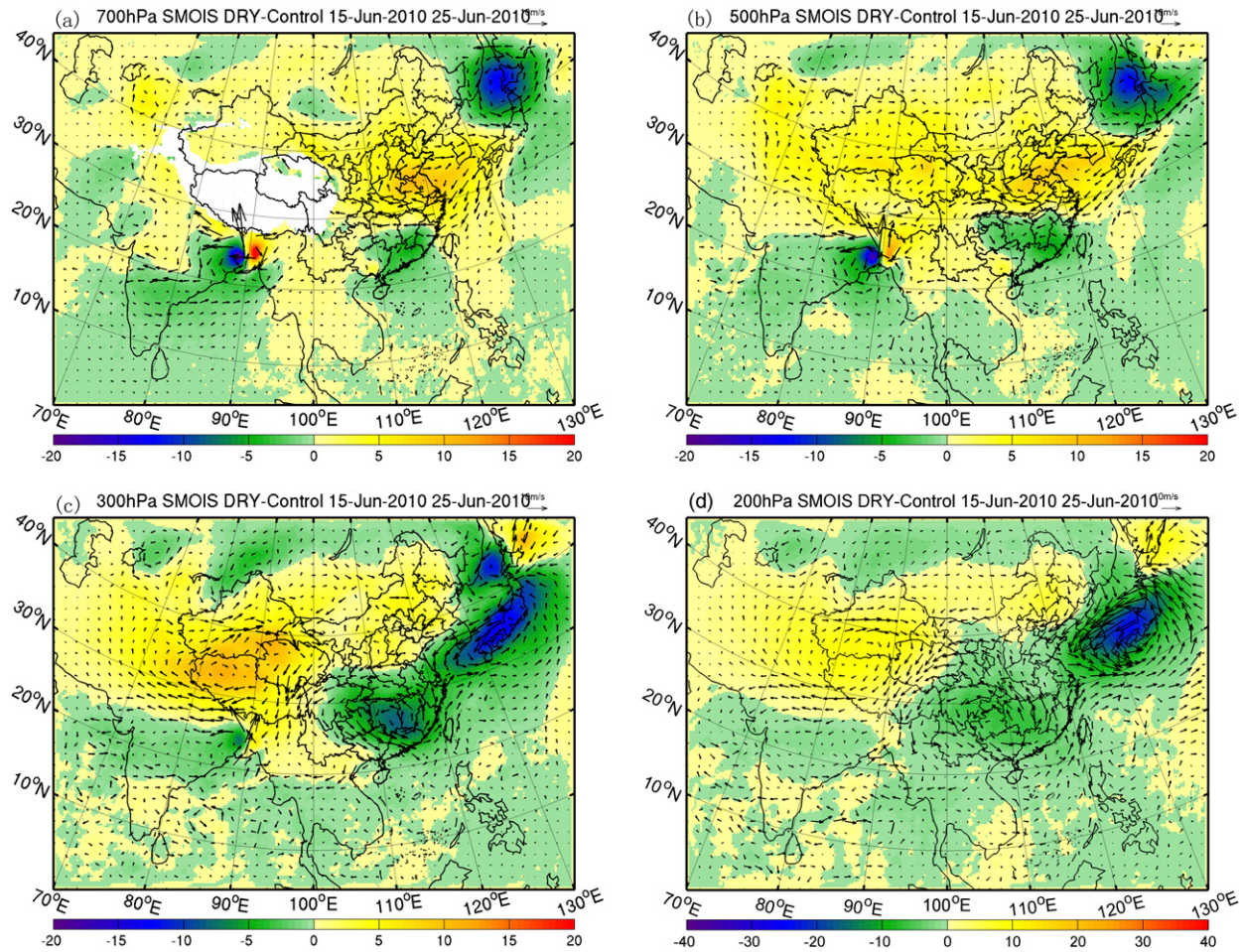


FIG. 12. Differences of geopotential height, wind speed, and direction between the DRY and CNTL cases during the precipitation period. Shading color for geopotential height difference and vectors for wind speed difference. (a) 700, (b) 500, (c) 300, and (d) 200 hPa.

significantly different from those in DRY. Inside of oscillating around 30°N, they were moving southward (yellow and brown line), consistent with the contour lines in 850 hPa. This result is consistent with the study of Li et al. (2014) but with a subtle difference. They accomplished the outcome by reducing the TP surface albedo to 1.0 to obtain a weaker surface heating, and showed that a weaker TP surface heating restrained the low pressure vortices over the eastern plateau and reduce the precipitation in southern China. While our results showed that a stronger TP surface heating enhances the high pressure anomaly in the north of the rain belt, blocks the northward movement of the low pressure in southern China, and increases the precipitation in southern China.

e. Water vapor transport

Ample water vapor supply is critical for persistent precipitation. The total water vapor transport is

calculated by integrating each layer's water vapor multiplied by wind speed from the bottom to the top. The control case shows the water vapor has two main sources: the Bay of Bengal and the South China Sea (Fig. 14c).

The enhanced TP surface heating in the DRY simulation not only enhanced the high pressure downstream, but also strengthened the low pressure in southern China (Figs. 12a and 12b) and finally changed the water vapor transport. As shown in Figs. 14a and 14b, the DRY simulation had a stronger vapor transport in southern China. A northward anomaly over southern China and a southward anomaly over the East China Sea can be found in the water vapor transfer difference between the DRY and CNTL case (Fig. 14b). These two anomalies result in a water vapor convergence anomaly in southern China in the DRY case (Fig. 14d). This also explained the decreased precipitation over Japan in DRY. Water vapor convergence provides ample water vapor and benefits

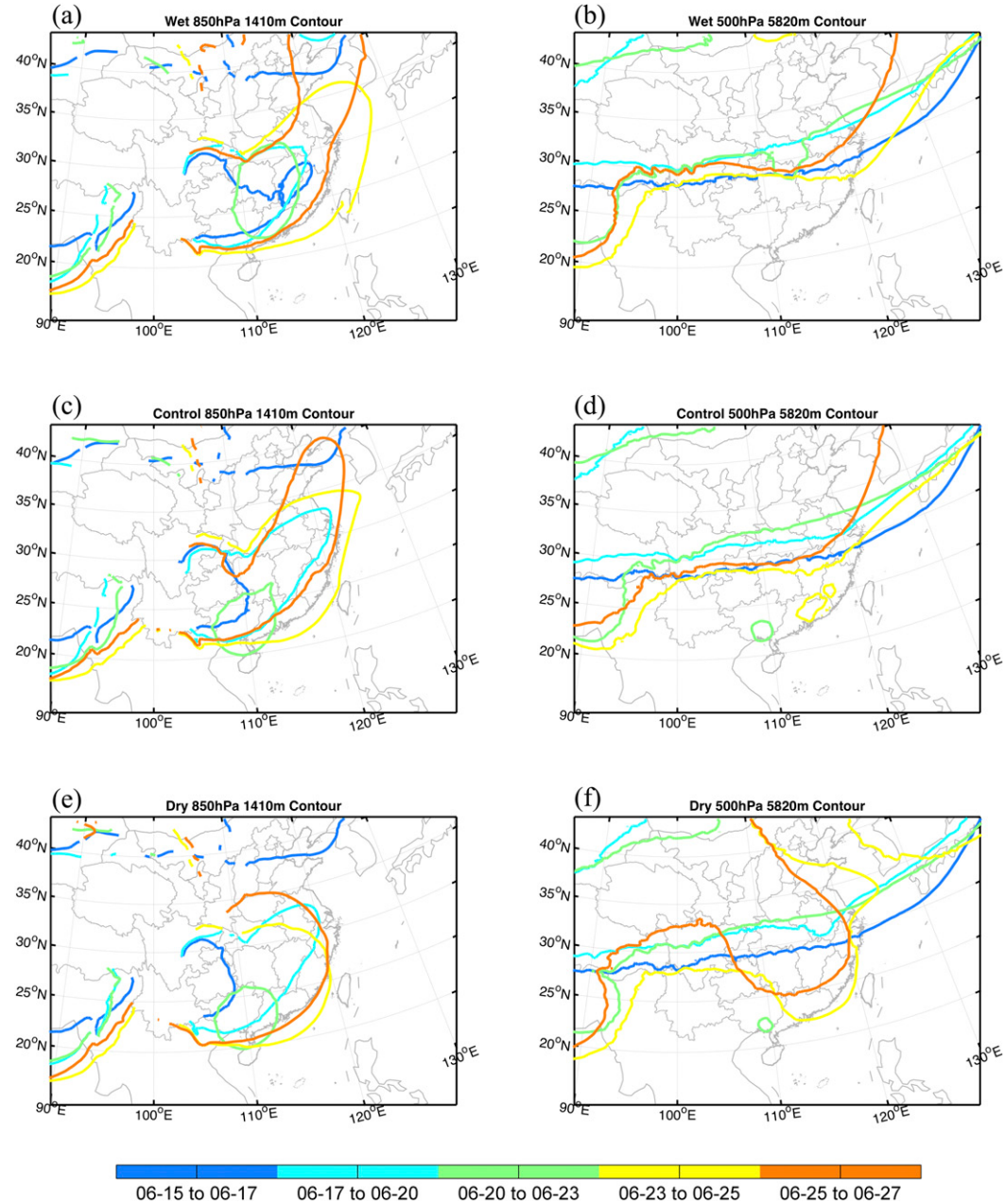


FIG. 13. (left) The 1410-m contour lines for 850 hPa and (right) the 5820-m contour lines for 500 hPa. (a),(b) WET; (c),(d) CNTL; and (e),(f) DRY.

convection. The similarity between the pattern of the water vapor convergence anomaly and the precipitation pattern in the DRY case (Fig. 8b) confirmed this.

The water vapor transport difference can be traced back to the circulation changing. As can be seen in Figs. 14b and 14f, the pattern of 10-m surface wind difference was generally similar to the pattern of water vapor transport in both orientation and intensity except over TP where land surface processes differ greatly between cases. The southward anomaly over the East

China Sea and the northward anomaly over southern China can also be found at 700 and 500 hPa (Figs. 12a and 12b). In conclusion, the enhanced high in the north of the precipitation belt prevented water vapor from moving to the north in the DRY simulation and the enhanced low pressure in southern China absorbed more water vapor from the South China Sea (Fig. 14b). Therefore, in DRY, more water vapor was concentrated in southern China, favoring the enhancement of extreme precipitation.

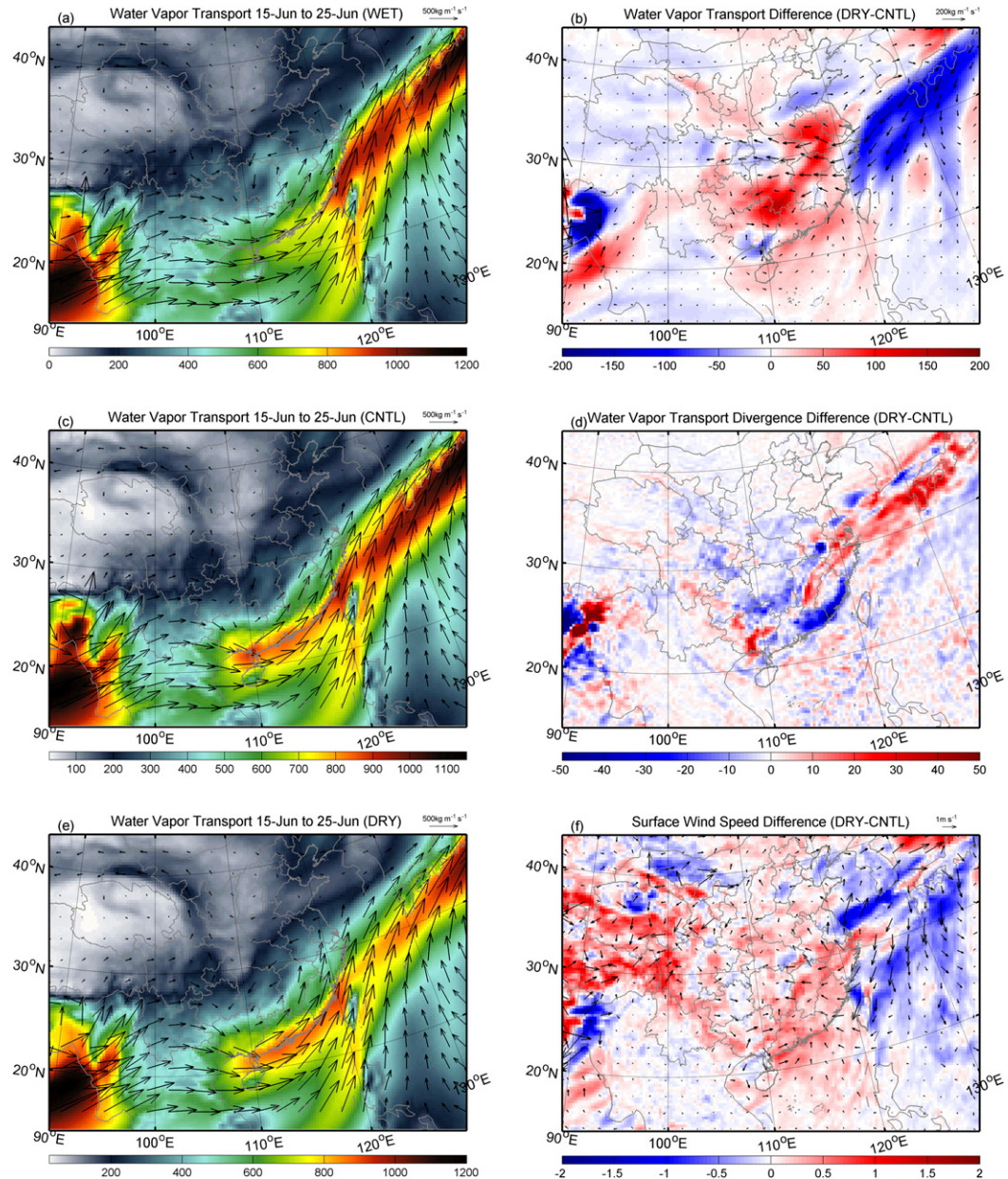


FIG. 14. (left) Water vapor transport ($\text{kg m}^{-1} \text{s}^{-1}$) of three different cases; shaded color is for absolute value. Vectors are for the water transport direction. The length of the arrow indicates the absolute value of the water transport amount. (a) WET, (c) CNTL, and (e) DRY. (right) The difference between the DRY and CNTL cases. (b) Water vapor transport difference ($\text{kg m}^{-1} \text{s}^{-1}$). (d) Water vapor convergence difference ($\text{kg m}^{-2} \text{day}^{-1}$). (f) 10-m wind difference ($\text{m} \text{s}^{-1}$).

The water vapor transport difference may also contribute to differences in the simulated diurnal cycle of precipitation (Fig. 8d) and the precipitation probability difference (Fig. 9). The afternoon precipitation is usually associated with convection, but the nighttime precipitation is often caused by stratiform clouds. The convective precipitation was short lived with heavy rainfall and the stratus precipitation was long lived with modest

rainfall intensity. With water vapor supply, the DRY case not only produced heavier daytime convection than DRY, but also produced more sustained nighttime precipitation. The WET case, however, is the lack of a water vapor supply. The convective precipitation was not as intensive as CNTL and DRY case. But it saved enough water vapor for nighttime precipitation. As a result, the WET case has lower precipitation during the daytime,

similar precipitation to the CNTL during nighttime, and has the most “light rainfall.”

6. Summary

By analyzing 10 persistent extreme precipitation events that occurred in the east part of southern China, we found that they have two common features. One is the TP surface has a warm anomaly prior to the onset of PEPEs, and the other is the existence of a significant high pressure anomaly north of the main rain belt. To understand the connection between these two features and to quantify the effects of the TP surface heating on PEPEs, three WRF sensitivity simulations were conducted with contrasting soil moisture conditions.

The WRF simulation with dry soil moisture produced the most intensive precipitation for that region, while the simulation with wet soil moisture has less precipitation. A weaker TP surface heating resulted in more light rainfall, accelerated the northward movement of the rain belt, and reduced the chance to develop PEPEs in the region of interest. Conversely, the DRY case, with greater heating over the TP surface, inhibited the light rain and promoted more extreme rainfall.

The TP's surface heating has two main effects on the development and evolution of PEPEs in southern China. The first one is connected to the generation of a cold air mass above the TP PBL due to updraft over the heated TP surface. This cold air mass is displaced toward the Yangtze Plain by the westerly flow, and thereby enhanced the high pressure underneath the cold air mass, which in turn blocks the movement of the low pressure system and strengthened low pressure, causing enhanced PEPEs in southern China.

The second one is associated with the enhancement of the water vapor transport from the South China Sea to the southern China. The strengthened low pressure in southern China absorbed more moisture from the South China Sea and the blocking high enhanced the accumulation of water vapor in the region. More moisture was then transported to southern China, which favored heavy precipitation generation.

The results of this study differ from the findings in a previous climate study because the time scales of interest are different. As documented in related climate studies, the TP heating works as a heat pump. A strong pump enhances the Asian summer monsoon and brings more water vapor northward. Our study suggests that the effects of TP surface heating for individual weather events may significantly differ from those for climatology. In climatology, the strong TP heating will push the rain belt to the north. However, if a high pressure occurs in the Yangtze Plain during the precipitation events, the

strong TP surface heating also strengthens the high anomaly, enhances the precipitation south of the high pressure, and blocks the northward movement of the precipitation. It seems that this effect only works on mesoscale systems, and it may not play an important role during the entire summer monsoon season.

Acknowledgments. This study is supported by the National Program on Key Basic Research Project of China (973) under Grant 2012CB417203 and the State Key Program of the National Natural Science Foundation of China under Grant 91537211. We appreciate the valuable comments from Drs. Guoxiong Wu and Jiangyu Mao.

REFERENCES

- Bao, Q., J. Yang, Y. Liu, G. Wu, and B. Wang, 2010: Roles of anomalous Tibetan Plateau warming on the severe 2008 winter storm in central-southern China. *Mon. Wea. Rev.*, **138**, 2375–2384, doi:[10.1175/2009MWR2950.1](https://doi.org/10.1175/2009MWR2950.1).
- Barlage, M., M. Tewari, F. Chen, G. Miguez-Macho, Z.-L. Yang, and G.-Y. Niu, 2015: The effect of groundwater interaction in North American regional climate simulations with WRF/Noah-MP. *Climatic Change*, **129**, 485–498, doi:[10.1007/s10584-014-1308-8](https://doi.org/10.1007/s10584-014-1308-8).
- Barnes, S. L., F. Caracena, and A. Marroquin, 1996: Extracting synoptic-scale diagnostic information from mesoscale models: The Eta model, gravity waves, and quasigeostrophic diagnostics. *Bull. Amer. Meteor. Soc.*, **77**, 519–528, doi:[10.1175/1520-0477\(1996\)077<0519:ESSDIF>2.0.CO;2](https://doi.org/10.1175/1520-0477(1996)077<0519:ESSDIF>2.0.CO;2).
- Boos, W. R., and Z. Kuang, 2010: Dominant control of the South Asian monsoon by orographic insulation versus plateau heating. *Nature*, **463**, 218–222, doi:[10.1038/nature08707](https://doi.org/10.1038/nature08707).
- Chen, F., and J. Dudhia, 2001: Coupling an advanced land surface-hydrology model with the Penn State–NCAR MM5 modeling system. Part I: Model implementation and sensitivity. *Mon. Wea. Rev.*, **129**, 569–585, doi:[10.1175/1520-0493\(2001\)129<0569:CAALSH>2.0.CO;2](https://doi.org/10.1175/1520-0493(2001)129<0569:CAALSH>2.0.CO;2).
- , and Coauthors, 2007: Description and evaluation of the characteristics of the NCAR high-resolution land data assimilation system. *J. Appl. Meteor. Climatol.*, **46**, 694–713, doi:[10.1175/JAM2463.1](https://doi.org/10.1175/JAM2463.1).
- Chen, Y., and P. Zhai, 2013: Persistent extreme precipitation events in China during 1951–2010. *Climate Res.*, **57**, 143–155, doi:[10.3354/cr01171](https://doi.org/10.3354/cr01171).
- China Meteorological Data Service Center, 2008: Dataset of daily climate data from Chinese surface stations for global exchange. Accessed 15 August 2014. [Available online at http://data.cma.cn/en/?r=data/detail&dataCode=SURF_CLI_CHN_MUL_DAY_CES.]
- Ding, Y., 1992: Summer monsoon rainfalls in China. *J. Meteor. Soc. Japan*, **70**, 373–396, doi:[10.2151/jmsj1965.70.1B_373](https://doi.org/10.2151/jmsj1965.70.1B_373).
- , and J. C. Chan, 2005: The East Asian summer monsoon: An overview. *J. Meteor. Atmos. Phys.*, **89**, 117–142, doi:[10.1007/s00703-005-0125-z](https://doi.org/10.1007/s00703-005-0125-z).
- Duan, A., and G. Wu, 2005: Role of the Tibetan Plateau thermal forcing in the summer climate patterns over subtropical Asia. *Climate Dyn.*, **24**, 793–807, doi:[10.1007/s00382-004-0488-8](https://doi.org/10.1007/s00382-004-0488-8).
- , and —, 2008: Weakening trend in the atmospheric heat source over the Tibetan Plateau during recent decades. Part I:

- Observations. *J. Climate*, **21**, 3149–3164, doi:[10.1175/2007JCLI1912.1](https://doi.org/10.1175/2007JCLI1912.1).
- , and —, 2009: Weakening trend in the atmospheric heat source over the Tibetan Plateau during recent decades. Part II: Connection with climate warming. *J. Climate*, **22**, 4197–4212, doi:[10.1175/2009JCLI2699.1](https://doi.org/10.1175/2009JCLI2699.1).
- , F. Li, M. Wang, and G. Wu, 2011: Persistent weakening trend in the spring sensible heat source over the Tibetan Plateau and its impact on the Asian summer monsoon. *J. Climate*, **24**, 5671–5682, doi:[10.1175/JCLI-D-11-00052.1](https://doi.org/10.1175/JCLI-D-11-00052.1).
- , M. Wang, Y. Lei, and Y. Cui, 2013: Trends in summer rainfall over China associated with the Tibetan Plateau sensible heat source during 1980–2008. *J. Climate*, **26**, 261–275, doi:[10.1175/JCLI-D-11-00669.1](https://doi.org/10.1175/JCLI-D-11-00669.1).
- Easterling, D. R., J. L. Evans, P. Ya. Groisman, T. R. Karl, K. E. Kunkel, and P. Ambenje, 2000: Observed variability and trends in extreme climate events: A brief review. *Bull. Amer. Meteor. Soc.*, **81**, 417–425, doi:[10.1175/1520-0477\(2000\)081<0417:OVATIE>2.3.CO;2](https://doi.org/10.1175/1520-0477(2000)081<0417:OVATIE>2.3.CO;2).
- Fennessy, M. J., and J. Shukla, 1999: Impact of initial soil wetness on seasonal atmospheric prediction. *J. Climate*, **12**, 3167–3180, doi:[10.1175/1520-0442\(1999\)012<3167:IOISWO>2.0.CO;2](https://doi.org/10.1175/1520-0442(1999)012<3167:IOISWO>2.0.CO;2).
- Gao, Y., K. Li, F. Chen, Y. Jiang, and C. Lu, 2015: Assessing and improving Noah-MP land model simulations for the central Tibetan Plateau. *J. Geophys. Res. Atmos.*, **120**, 9258–9278, doi:[10.1002/2015JD023404](https://doi.org/10.1002/2015JD023404).
- Grell, G. A., and S. R. Freitas, 2014: A scale and aerosol aware stochastic convective parameterization for weather and air quality modeling. *Atmos. Chem. Phys.*, **14**, 5233–5250, doi:[10.5194/acp-14-5233-2014](https://doi.org/10.5194/acp-14-5233-2014).
- Hong, S.-Y., and J.-O. J. Lim, 2006: The WRF Single-Moment-Microphysics Scheme Class 6 (WSM6). *J. Korean Meteor. Soc.*, **42**, 362–363.
- , Y. Noh, and J. Dudhia, 2006: A new vertical diffusion package with an explicit treatment of entrainment processes. *Mon. Wea. Rev.*, **134**, 2318–2341, doi:[10.1175/MWR3199.1](https://doi.org/10.1175/MWR3199.1).
- Huffman, G. J., and D. T. Bolvin, 2017: Real-Time TRMM Multi-Satellite Precipitation Analysis data set documentation. Accessed 11 May 2017. [Available online at https://pmm.nasa.gov/sites/default/files/document_files/3B4XRT_doc_V7_4_19_17.pdf.]
- Iacono, M. J., J. S. Delamere, E. J. Mlawer, M. W. Shephard, S. A. Clough, and W. D. Collins, 2008: Radiative forcing by long-lived greenhouse gases: Calculations with the AER radiative transfer models. *J. Geophys. Res.*, **113**, D13103, doi:[10.1029/2008JD009944](https://doi.org/10.1029/2008JD009944).
- Jiang, D., Z. Ding, H. Drange, and Y. Gao, 2008: Sensitivity of East Asian climate to the progressive uplift and expansion of the Tibetan Plateau under the mid-Pliocene boundary conditions. *Adv. Atmos. Sci.*, **25**, 709–722, doi:[10.1007/s00376-008-0709-x](https://doi.org/10.1007/s00376-008-0709-x).
- Jones, C., 2000: Occurrence of extreme precipitation events in California and relationships with the Madden-Julian Oscillation. *J. Climate*, **13**, 3576–3587, doi:[10.1175/1520-0442\(2000\)013<3576:OOEPEI>2.0.CO;2](https://doi.org/10.1175/1520-0442(2000)013<3576:OOEPEI>2.0.CO;2).
- Kalnay, E., and Coauthors, 1996: The NCEP/NCAR 40-Year Reanalysis Project. *Bull. Amer. Meteor. Soc.*, **77**, 437–471, doi:[10.1175/1520-0477\(1996\)077<0437:TNYRP>2.0.CO;2](https://doi.org/10.1175/1520-0477(1996)077<0437:TNYRP>2.0.CO;2).
- Koster, R. D., and M. J. Suarez, 2001: Soil moisture memory in climate models. *J. Hydrometeor.*, **2**, 558–570, doi:[10.1175/1525-7541\(2001\)002<0558:SMMCIM>2.0.CO;2](https://doi.org/10.1175/1525-7541(2001)002<0558:SMMCIM>2.0.CO;2).
- Kunkel, K. E., D. R. Easterling, K. Redmond, and K. Hubbard, 2003: Temporal variations of extreme precipitation events in the United States: 1895–2000. *Geophys. Res. Lett.*, **30**, 1900, doi:[10.1029/2003GL018052](https://doi.org/10.1029/2003GL018052).
- , —, D. A. R. Kristovich, B. Gleason, L. Stoecker, and R. Smith, 2012: Meteorological causes of the secular variations in observed extreme precipitation events for the conterminous United States. *J. Hydrometeor.*, **13**, 1131–1141, doi:[10.1175/JHM-D-11-0108.1](https://doi.org/10.1175/JHM-D-11-0108.1).
- Lawrence, D. M., and J. M. Slingo, 2005: Weak land–atmosphere coupling strength in HadAM3: The role of soil moisture variability. *J. Hydrometeor.*, **6**, 670–680, doi:[10.1175/JHM445.1](https://doi.org/10.1175/JHM445.1).
- Lee, J. Y., B. Wang, M. C. Wheeler, X. Fu, D. E. Waliser, and I. S. Kang, 2013: Real-time multivariate indices for the boreal summer intraseasonal oscillation over the Asian summer monsoon region. *Climate Dyn.*, **40**, 493–509, doi:[10.1007/s00382-012-1544-4](https://doi.org/10.1007/s00382-012-1544-4).
- Li, H., A. Dai, T. Zhou, and J. Lu, 2010: Responses of East Asian summer monsoon to historical SST and atmospheric forcing during 1950–2000. *Climate Dyn.*, **34**, 501–514, doi:[10.1007/s00382-008-0482-7](https://doi.org/10.1007/s00382-008-0482-7).
- Li, T., Y. Zhang, C. P. Chang, and B. Wang, 2001: On the relationship between Indian Ocean sea surface temperature and Asian summer monsoon. *Geophys. Res. Lett.*, **28**, 2843–2846, doi:[10.1029/2000GL011847](https://doi.org/10.1029/2000GL011847).
- Li, X., Y. Luo, and Z. Guan, 2014: The persistent heavy rainfall over southern China in June 2010: Evolution of synoptic systems and the effects of the Tibetan Plateau heating. *J. Meteor. Res.*, **28**, 540–560, doi:[10.1007/s13351-014-3284-3](https://doi.org/10.1007/s13351-014-3284-3).
- Liu, H., D.-L. Zhang, and B. Wang, 2008: Daily to submonthly weather and climate characteristics of the summer 1998 extreme rainfall over the Yangtze River Basin. *J. Geophys. Res.*, **113**, D22101, doi:[10.1029/2008JD010072](https://doi.org/10.1029/2008JD010072).
- Liu, X., and Z.-Y. Yin, 2002: Sensitivity of East Asian monsoon climate to the uplift of the Tibetan Plateau. *Palaeogeogr. Palaeoclimatol. Palaeoecol.*, **183**, 223–245, doi:[10.1016/S0031-0182\(01\)00488-6](https://doi.org/10.1016/S0031-0182(01)00488-6).
- Liu, Y., G. Wu, J. Hong, B. Dong, A. Duan, Q. Bao, and L. Zhou, 2012: Revisiting Asian monsoon formation and change associated with Tibetan Plateau forcing: II. Change. *Climate Dyn.*, **39**, 1183–1195, doi:[10.1007/s00382-012-1335-y](https://doi.org/10.1007/s00382-012-1335-y).
- Mao, J., Z. Sun, and G. Wu, 2010: 20–50-day oscillation of summer Yangtze rainfall in response to intraseasonal variations in the subtropical high over the western North Pacific and South China Sea. *Climate Dyn.*, **34**, 747–761, doi:[10.1007/s00382-009-0628-2](https://doi.org/10.1007/s00382-009-0628-2).
- Mintz, Y., 1982: The sensitivity of numerically simulated climates to land surface conditions. *Land Surface Processes in Atmospheric General Circulation Models*, P. S. Eagleson, Ed., Cambridge University Press, 109–111.
- Mooney, C. Z., and R. D. Duval, 1993: *Bootstrapping: A Non-parametric Approach to Statistical Inference (Quantitative Applications in the Social Sciences)*. SAGE Publications, Inc., 80 pp.
- NOAA/NWS/NCEP, 2000: NCEP FNL Operational Model Global Tropospheric Analyses, continuing from July 1999. Research Data Archive at the National Center for Atmospheric Research, Computational and Information Systems Laboratory, accessed 30 May 2015. [Available online at <http://rda.ucar.edu/datasets/ds083.2/>.]
- NCEP Climate Prediction Center and UCAR Joint Office for Science Support, 2000: NCEP/CPC Four-Kilometer Precipitation Set, Gauge, and Radar (updated quarterly). Research Data Archive at the National Center for Atmospheric Research, Computational and Information Systems Laboratory, accessed 20 October 2016. [Available online at <https://rda.ucar.edu/datasets/ds507.5/>.]

- Niu, G. Y., and Z. L. Yang, 2004: Effects of vegetation canopy processes on snow surface energy and mass balances. *J. Geophys. Res.*, **109**, D23111, doi:[10.1029/2004JD004884](https://doi.org/10.1029/2004JD004884).
- , and Coauthors, 2011: The community Noah land surface model with multiparameterization options (Noah-MP): 1. Model description and evaluation with local-scale measurements. *J. Geophys. Res.*, **116**, D12109, doi:[10.1029/2010JD015139](https://doi.org/10.1029/2010JD015139).
- Noilhan, J., and S. Planton, 1989: A simple parameterization of land surface processes for meteorological models. *Mon. Wea. Rev.*, **117**, 536–549, doi:[10.1175/1520-0493\(1989\)117<0536:ASPOL>2.0.CO;2](https://doi.org/10.1175/1520-0493(1989)117<0536:ASPOL>2.0.CO;2).
- Pan, W., J. Mao, and G. Wu, 2013: Characteristics and mechanism of the 10–20-day oscillation of spring rainfall over southern China. *J. Climate*, **26**, 5072–5087, doi:[10.1175/JCLI-D-12-00618.1](https://doi.org/10.1175/JCLI-D-12-00618.1).
- Pan, Z., E. Takle, M. Segal, and R. Turner, 1996: Influences of model parameterization schemes on the response of rainfall to soil moisture in the central United States. *Mon. Wea. Rev.*, **124**, 1786–1802, doi:[10.1175/1520-0493\(1996\)124<1786:IOMP>2.0.CO;2](https://doi.org/10.1175/1520-0493(1996)124<1786:IOMP>2.0.CO;2).
- Ren, X. J., X. Q. Yang, and X. Sun, 2013: Zonal oscillation of western Pacific subtropical high and subseasonal SST variations during Yangtze persistent heavy rainfall events. *J. Climate*, **26**, 8929–8946, doi:[10.1175/JCLI-D-12-00861.1](https://doi.org/10.1175/JCLI-D-12-00861.1).
- Rodell, M., and Coauthors, 2004: The Global Land Data Assimilation System. *Bull. Amer. Meteor. Soc.*, **85**, 381–394, doi:[10.1175/BAMS-85-3-381](https://doi.org/10.1175/BAMS-85-3-381).
- Stéfanon, M., P. Drobinski, F. D'Andrea, C. Lebeaupin-Brossier, and S. Bastin, 2014: Soil moisture-temperature feedbacks at meso-scale during summer heat waves over Western Europe. *Climate Dyn.*, **42**, 1309–1324, doi:[10.1007/s00382-013-1794-9](https://doi.org/10.1007/s00382-013-1794-9).
- Trier, S. B., F. Chen, and K. W. Manning, 2004: A study of convection initiation in a mesoscale model using high-resolution land surface initial conditions. *Mon. Wea. Rev.*, **132**, 2954–2976, doi:[10.1175/MWR2839.1](https://doi.org/10.1175/MWR2839.1).
- , M. A. LeMone, F. Chen, and K. W. Manning, 2011: Effects of surface heat and moisture exchange on ARW-WRF warm-season precipitation forecasts over the central United States. *Wea. Forecasting*, **26**, 3–25, doi:[10.1175/2010WAF2222426.1](https://doi.org/10.1175/2010WAF2222426.1).
- Wang, B., Q. Bao, B. Hoskins, G. Wu, and Y. Liu, 2008: Tibetan Plateau warming and precipitation changes in East Asia. *Geophys. Res. Lett.*, **35**, L14702, doi:[10.1029/2008GL034330](https://doi.org/10.1029/2008GL034330).
- Wang, Y., and L. Zhou, 2005: Observed trends in extreme precipitation events in China during 1961–2001 and the associated changes in large scale circulation. *Geophys. Res. Lett.*, **32**, L17708, doi:[10.1029/2005GL023769](https://doi.org/10.1029/2005GL023769).
- Wang, Z., A. Duan, and G. Wu, 2014: Time-lagged impact of spring sensible heat over the Tibetan Plateau on the summer rainfall anomaly in East China: Case studies using the WRF model. *Climate Dyn.*, **42**, 2885–2898, doi:[10.1007/s00382-013-1800-2](https://doi.org/10.1007/s00382-013-1800-2).
- Wilks, D. S., 2006: *Statistical Methods in the Atmosphere Sciences*. Vol. 100, 2nd ed. Elsevier, 648 pp.
- Wu, G., and Y. Zhang, 1998: Tibetan Plateau forcing and the timing of the monsoon onset over South Asia and the South China Sea. *Mon. Wea. Rev.*, **126**, 913–927, doi:[10.1175/1520-0493\(1998\)126<0913:TPFATT>2.0.CO;2](https://doi.org/10.1175/1520-0493(1998)126<0913:TPFATT>2.0.CO;2).
- , W. Li, H. Guo, and H. Liu, 1997: Sensible heating-drive air pump of the Tibetan Plateau and the Asian summer monsoon. *Memorial Volume of Prof. J.Z. Zhao*, Y. Duzheng, Ed., Science Press, Beijing, 116–126.
- , Y. Liu, B. He, Q. Bao, A. Duan, and F. F. Jin, 2012a: Thermal controls on the Asian summer monsoon. *Sci. Rep.*, **2**, 404, doi:[10.1038/srep00404](https://doi.org/10.1038/srep00404).
- , —, B. Dong, X. Liang, A. Duan, Q. Bao, and J. Yu, 2012b: Revisiting Asian monsoon formation and change associated with Tibetan Plateau forcing: I. Formation. *Climate Dyn.*, **39**, 1169–1181, doi:[10.1007/s00382-012-1334-z](https://doi.org/10.1007/s00382-012-1334-z).
- Wu, W., and R. W. Dickinson, 2004: Time scales of layered soil moisture memory in the context of land–atmosphere interaction. *J. Climate*, **17**, 2752–2764, doi:[10.1175/1520-0442\(2004\)017<2752:TSOLSM>2.0.CO;2](https://doi.org/10.1175/1520-0442(2004)017<2752:TSOLSM>2.0.CO;2).
- Xu, Z. Q., K. Fan, and H. J. Wang, 2015: Decadal variation of summer precipitation over China and associated atmospheric circulation after the late 1990s. *J. Climate*, **28**, 4086–4106, doi:[10.1175/JCLI-D-14-00464.1](https://doi.org/10.1175/JCLI-D-14-00464.1).
- Yanai, M., C. Li, and Z. Song, 1992: Seasonal heating of the Tibetan Plateau and its effects on the evolution of the Asian summer monsoon. *J. Meteor. Soc. Japan*, **70**, 319–351, doi:[10.2151/jmsj1965.70.1B_319](https://doi.org/10.2151/jmsj1965.70.1B_319).
- Yang, Z. L., and Coauthors, 2011: The community Noah land surface model with multiparameterization options (Noah-MP): 2. Evaluation over global river basins. *J. Geophys. Res.*, **116**, D12110, doi:[10.1029/2010JD015140](https://doi.org/10.1029/2010JD015140).
- Ye, D., and G. Wu, 1998: The role of the heat source of the Tibetan Plateau in the general circulation. *Meteor. Atmos. Phys.*, **67**, 181–198, doi:[10.1007/BF01277509](https://doi.org/10.1007/BF01277509).
- Yu, R., B. Wang, and T. Zhou, 2004: Tropospheric cooling and summer monsoon weakening trend over East Asia. *Geophys. Res. Lett.*, **31**, L22212, doi:[10.1029/2004GL021270](https://doi.org/10.1029/2004GL021270).
- Zhang, G., F. Chen, and Y. Gan, 2016: Assessing uncertainties in the Noah-MP ensemble simulations of a cropland site during the Tibet Joint International Cooperation program field campaign. *J. Geophys. Res. Atmos.*, **121**, 9576–9596, doi:[10.1002/2016JD024928](https://doi.org/10.1002/2016JD024928).
- Zhisheng, A., J. E. Kutzbach, W. L. Prell, and S. Porter, 2001: Evolution of Asian monsoons and phased uplift of the Himalaya–Tibetan plateau since Late Miocene times. *Nature*, **411**, 62–66, doi:[10.1038/35075035](https://doi.org/10.1038/35075035).
- Zuo, Z., S. Yang, R. Zhang, P. Jiang, L. Zhang, and F. Wang, 2013: Long-term variations of broad-scale Asian summer monsoon circulation and possible causes. *J. Climate*, **26**, 8947–8961, doi:[10.1175/JCLI-D-12-00691.1](https://doi.org/10.1175/JCLI-D-12-00691.1).